Chapter 4

Numerical Method for SHF plus RPA approach in three-dimensional Cartesian mesh representation

In this chapter, we explain the numerical solution of Skyrme Hartree-Fock (SHF) plus random phase approximation (RPA) approach in three-dimensional (3D) Cartesian mesh representation and we examine the numerical accuracy of our formulation. We simply call the three-dimensional (3D) Cartesian mesh representation the "mesh representation" in this chapter.

Our numerical procedure consists of two steps: First, we solve the SHF equation in order to obtain the single-particle wave functions and single-particle energies. Second, we solve the RPA equation, which is constructed from the obtained single-particle wave functions and single-particle energies, in order to obtain the RPA wave function and excitation energies. We perform the 3D Cartesian mesh calculation when we solve the SHF equation and the RPA equation.

In section 4.1, we explain the techniques made use of in solving the SHF equation in the mesh representation. The various techniques used in the SHF calculation are almost entirely applied to the RPA calculation. In section 4.2, we explain the techniques to solve the RPA equation in the mesh representation. The RPA calculation in the mesh representation is almost analogous to the SHF calculation in the mesh representation. In section 4.3, we present the method for obtaining the accurate results. In section 4.4, we propose a method for obtaining the RPA correlation energy of spurious mode in terms of our formulation. In section 4.5, we compare our results with the ones by other's calculations. In section 4.6, we make comment on the instability due

to the $\boldsymbol{s} \cdot \Delta \boldsymbol{s}$ terms in Skyrme energy functional.

4.1 Skyrme Hartree-Fock calculation in the mesh representation

In this section, we explain the techniques employed in solving the SHF equation in the mesh representation. We restrict ourselves to the case for even-even triaxial nuclei. We assume the time-reversal invariance of the density and the HF hamiltonian. Then, we can construct the time-reversal pair of the single-particle wave functions in Eq. (3.62). The SHF equations (3.69) for such time-reversal pair of the single-particle wave functions are already introduced in section 3.4. The SHF equation is solved for one member of the pair. Since we can impose the symmetries with respect to reflection in $x = 0$, $y = 0$ and $z = 0$-planes on the density, we can also impose the spatial symmetries on the single-particle wave function. It enables us to carry out the calculations in one eighth of the total mesh space when the SHF equation is solved.

In subsection 4.1.1, we explain the treatment of the Skyrme energy functional in the variational formulation. From the Skyrme energy functional the HF equation and the RPA equation are derived through variation with respect to density matrix. In subsection 4.1.2, we briefly explain the Lagrange mesh method, which is used in order to approximate the differential operators in the mesh calculation. In subsection 4.1.3, we explain the iterative solution of Hartree-Fock equation in the mesh representation. In subsection 4.1.4, we explain how we impose the spatial symmetry on the single-particle wave functions. In subsection 4.1.5, we introduce the method for calculating the Coulomb potential in Ref. [24].

4.1.1 Treatment of the Skyrme energy functional

In this section, we explain the treatment of the center of mass correction for the spurious motion in Eq. (3.2). We also explain the removed terms in energy functional for each of the Skyrme force used in our calculation.

The center of mass correction for the spurious motion is necessary to evaluate the binding energy of nucleus. There are two types of ways of corrections. One of them is the variation after projection (VAP) and the other is the projection after variation (PAV) (cf. [57]). The center of mass energy is given as

$$E_{\text{c.m.}} = -\frac{\langle \text{HF}|\hat{P}^2_{\text{c.m.}}|\text{HF}\rangle}{2Am}, \tag{4.1}$$

where $\hat{P}_{\text{c.m.}} = \sum_i \hat{p}_i$ is total momentum. In the case of VAP, the variation involving the center of mass correction $\delta(E_{\text{int}} - E_{\text{c.m.}})$ is done and the binding energy is $E = \mathcal{E} - E_{\text{c.m.}}$. Because the variation $\delta E_{\text{c.m.}}$ is numerically complicated, the center of mass energy is approximated by

$$E_{\text{c.m.}} \simeq -\frac{\hbar^2}{2Am} \sum_{i,\sigma\tau} \int \mathrm{d}\boldsymbol{r}\, \phi_i^*(\boldsymbol{r}\sigma\tau) \triangle \phi_i(\boldsymbol{r}\sigma\tau) = \frac{\hbar^2}{2Am} \int \mathrm{d}\boldsymbol{r}\, \tau(\boldsymbol{r}). \tag{4.2}$$

Then, we can put the center of mass correction into the kinetic energy functional $\mathcal{E}_{\text{kin}}$ in Eq. (3.3):

$$\mathcal{E}_{\text{kin}} = \frac{\hbar^2}{2m} \left(1 - \frac{1}{A}\right) \tau. \tag{4.3}$$

Thus, the VAP becomes a simple variation $\delta E = \delta E_{\text{int}}$.

In the case of PAV, a variation δE_{int} is done and the binding energy is $E = E_{\text{int}} - E_{\text{c.m.}}$. PAV is appropriate to the Skyrme-Hartree-Fock plus RPA approach because the center of mass energy $E_{\text{c.m.}}$ of Eq. (4.2) coincides with the RPA correlation energy for the spurious center of mass vibration in Eq. (2.22). Getting together the above two handling method in terms of a switching parameter $\theta_{\text{c.m.}}$, the kinetic energy functional can be written as

$$\mathcal{E}_{\text{kin}} = \frac{\hbar^2}{2m} \left(1 - (1 - \theta_{\text{c.m.}}) \frac{1}{A}\right) \tau. \tag{4.4}$$

Then, a variation can be written as δE_{int} and the binding energy can be given as

$$E = E_{\text{int}} + \theta_{\text{c.m.}} \frac{\langle \text{HF} | \hat{P}^2_{\text{c.m.}} | \text{HF} \rangle}{2Am}, \tag{4.5}$$

where switching parameter $\theta_{\text{c.m}}$ is defined as

$$\theta_{\text{c.m.}} = \begin{cases} 0 & (\text{for VAP}) \\ 1 & (\text{for PAV}) \end{cases}. \tag{4.6}$$

For several Skyrme forces (for example, SIII, SkI4, and so on), the $\overleftrightarrow{J}^2$ terms in the Skyrme energy functional are neglected in the procedure of determining the parameter set. Because of the gauge invariance [58], the time-odd $\boldsymbol{s} \cdot \boldsymbol{T}$ terms are combined with the time-even $\overleftrightarrow{J}^2$ terms. So, if the $\overleftrightarrow{J}^2$ terms are neglected, then the $\boldsymbol{s} \cdot \boldsymbol{T}$ terms must be removed. Therefore, the coefficients C_t^T of $\left(\boldsymbol{s}_t \cdot \boldsymbol{T}_t - \overleftrightarrow{J}^2_t\right)$ term in Eq. (3.29) is changed in terms of a switching parameter θ_{J^2} into

$$\begin{aligned} C_0^T &= \theta_{J^2} \left[-\tfrac{1}{8} t_1 \left(\tfrac{1}{2} - x_1\right) + \tfrac{1}{8} t_2 \left(\tfrac{1}{2} + x_2\right)\right], \\ C_1^T &= \theta_{J^2} \left[-\tfrac{1}{16} t_1 + \tfrac{1}{16} t_2\right], \end{aligned}$$

where $\theta_{J^2} = 0$ or 1.

For Skyrme SkX forces, the exchange contribution of Coulomb interaction is neglected. We introduce switching parameter $\theta_{\mathrm{C,ex}}$ as

$$\mathcal{E}_{\mathrm{Coul,ex}}(\boldsymbol{r}) = -\theta_{\mathrm{C,ex}} \frac{3e^2}{4} \left(\frac{3}{\pi}\right)^{1/3} \rho_{\mathrm{p}}^{4/3}(\boldsymbol{r}), \tag{4.7}$$

where $\theta_{\mathrm{C,ex}} = 0$ or 1

For several Skyrme forces (for example, SkI4, SkO and so on), there occurs the instability for RPA calculation by $\boldsymbol{s}\cdot\triangle\boldsymbol{s}$ term in Skyrme energy functional (see section 4.?). In order to avoid this instability, the coefficients $C_t^{\triangle s}$ of $\boldsymbol{s}_t \cdot \triangle \boldsymbol{s}_t$ term in Eq. (3.29) is changed in terms of a switching parameter $\theta_{\triangle s}$ into

$$\begin{aligned} C_0^{\triangle s} &= \theta_{\triangle s}\left[\tfrac{3}{32}t_1\left(\tfrac{1}{2} - x_1\right) + \tfrac{1}{32}t_2\left(\tfrac{1}{2} + x_2\right)\right], \\ C_1^{\triangle s} &= \theta_{\triangle s}\left[\tfrac{3}{64}t_1 + \tfrac{1}{64}t_2\right], \end{aligned}$$

where $\theta_{\triangle s} = 0$ or 1.

Table 4.1 shows additional parameters of Skyrme forces used in this thesis.

Table 4.1: Additional parameters of Skyrme forces used in this thesis. The values of the mass of the nucleon is referred to Ref. [59].

Force	$\hbar^2/2m$	$\theta_{\mathrm{c.m.}}$	θ_{J^2}	$\theta_{\mathrm{C,ex}}$	$\theta_{\triangle s}$
SII,..,SV [8]	20.73553	0	0	1	1
SkM* [9]	20.7525	0	0	1	1
SGII [18]	20.7525	0	0	1	1
Z_σ [11]	20.7525	1	1	1	1
SkI4 [12]	20.7525	1	0	1	0
SkO [23]	20.73553	1	0	1	0
SkX [14]	20.73	1	1	0	0

4.1.2 Lagrange mesh method

The Lagrange mesh method is proposed by Baye and Heenen [27]. In the method, quantities are expressed on discretized spatial mesh. This method is suitable for variational calculations in a high accuracy.

In 3D mesh calculation, the mesh sizes and the number of the mesh points for each of the direction are given at the beginning in order to determine the

mesh space used in the calculation. In this thesis, we use the same mesh size h given in fm and the number of mesh points n for all of the directions, that is, we perform the calculation in the cubic box, where the length of the side of the cubic box is $L = n \times h$. We take the intervals of x, y and z as $(-L/2, L/2)$. Then, the position of the mesh point is expressed as

$$x_k = \tfrac{1}{2}(2k - n - 1)h, \qquad k = 1, \ldots, n, \tag{4.8a}$$
$$y_l = \tfrac{1}{2}(2l - n - 1)h, \qquad l = 1, \ldots, n, \tag{4.8b}$$
$$z_m = \tfrac{1}{2}(2m - n - 1)h, \qquad m = 1, \ldots, n. \tag{4.8c}$$

According to the Lagrange mesh method, the single-particle wave function in Eq. (3.69) is represented as

$$\phi_i(x, y, z, \sigma, q) = \sum_{k=1}^{n} \sum_{l=1}^{n} \sum_{m=1}^{n} f_k(x) f_l(y) f_m(z) \phi_i(x_k, y_l, z_m, \sigma, q), \tag{4.9}$$

with the Lagrange function given as

$$f_k(x) = \frac{1}{n} \frac{\sin[\pi(x - x_k)/h]}{\sin[\pi(x - x_k)/L]}. \tag{4.10}$$

The Lagrange function $f_k(x)$ has the two properties:

$$f_k(x_{k'}) = \delta_{kk'}, \tag{4.11}$$

and

$$\int_{-L/2}^{L/2} f_k(x) f_{k'}(x) \mathrm{d}x = h\delta_{kk'}. \tag{4.12}$$

The single-particle wave function $\phi_i(\boldsymbol{r}\sigma q)$ can be expanded in terms of the orthogonal basis function $f_{klm}(x, y, z) \equiv f_k(x) f_l(y) f_m(z)$ with the expansion coefficient $\phi_i(x_k, y_l, z_m, \sigma, q)$, which is the values of the single-particle wave function at the mesh point (x_k, y_l, z_m). That is, the single-particle wave function at a mesh point is the expansion coefficient in a orthogonal basis functions. Therefore, the equation for the single-particle wave function in the mesh representation is expressed as the equation for the expansion coefficient in a basis function $f_{klm}(x, y, z)$.

The inner product of the single-particle wave functions is given by

$$\begin{aligned} &\sum_{\sigma q} \int_{-L/2}^{L/2} \int_{-L/2}^{L/2} \int_{-L/2}^{L/2} \phi_i^*(x, y, z, \sigma, q) \phi_j(x, y, z, \sigma, q) \mathrm{d}x \mathrm{d}y \mathrm{d}z \\ &= \sum_{\sigma q} \sum_{klm} \phi_i^*(x_k, y_l, z_m, \sigma, q) \phi_j(x_k, y_l, z_m, \sigma, q) h^3. \end{aligned} \tag{4.13}$$

So, we can see that the mid-point rule of integration is exact for the product of the two wave functions. We approximate the expectation values of local quantity $F(\boldsymbol{r})$ as

$$\sum_{i\sigma q}\int_{-L/2}^{L/2}\int_{-L/2}^{L/2}\int_{-L/2}^{L/2}\phi_i^*(x,y,z,\sigma,q)F(x,y,z)\phi_i(x,y,z,\sigma,q)\mathrm{d}x\mathrm{d}y\mathrm{d}z$$
$$\approx\sum_{i\sigma q}\sum_{klm}\phi_i^*(x_k,y_l,z_m,\sigma,q)F(x_k,y_l,z_m)\phi_i(x_k,y_l,z_m,\sigma,q)h^3. \tag{4.14}$$

Thus, the product of the local quantity $F(\boldsymbol{r})$ and the single-particle wave function $\phi_i(\boldsymbol{r}\sigma q)$ is approximated by

$$F(x,y,z)\phi_i(x,y,z,\sigma,q)\approx\sum_{klm}f_k(x)f_l(y)f_m(z)F(x_k,y_l,z_m)\phi_i(x_k,y_l,z_m,\sigma,q). \tag{4.15}$$

The ν-th order derivative of the single-particle wave function with respect to x is given as

$$\frac{\partial^\nu}{\partial x^\nu}\phi_i(x,y,z,\sigma,q)=\sum_{klm}f_k^{(\nu)}(x)f_l(y)f_m(z)\phi_i(x_k,y_l,z_m,\sigma,q). \tag{4.16}$$

Then, the first and the second-order derivatives of the single-particle wave function with respect to x at the position (x_k,y_l,z_m) are given as

$$\left.\frac{\partial^\nu}{\partial x^\nu}\phi_i(x,y_l,z_m,\sigma,q)\right|_{x=x_k}=\sum_{k'}D_{kk'}^{(\nu)}\phi_i(x_{k'},y_l,z_m,\sigma,q),\qquad \nu=1,2, \tag{4.17}$$

with the matrices $D_{kk'}^{(\nu)}$ approximating the differential operator

$$D_{kk'}^{(1)}=\begin{cases}0, & k=k',\\ (-1)^{k-k'}\dfrac{\pi}{L}\dfrac{1}{\sin[\pi(x_k-x_{k'})/L]}, & k\neq k',\end{cases} \tag{4.18a}$$

$$D_{kk'}^{(2)}=\begin{cases}-\dfrac{\pi^2}{3}\left(1-\dfrac{1}{L^2}\right), & k=k',\\ (-1)^{k-k'+1}\dfrac{2\pi^2}{L^2}\dfrac{\cos[\pi(x_k-x_{k'})/L]}{\sin^2[\pi(x_k-x_{k'})/L]}, & k\neq k'.\end{cases} \tag{4.18b}$$

The numerical error of the derivative of the function in Eq. (4.18) is much smaller than those of the finite difference formulae [27, 60]. In section 4.3, we display the difference between the numerical results using Eq. (4.18) and

those using 9-point formula of finite difference method in the SHF plus RPA calculation.

In terms of Eqs. (4.15) and (4.17), we can discretise the SHF equation (3.73):

$$\sum_{k'l'm'\sigma'} h_q(\boldsymbol{r}_{klm}\sigma;\boldsymbol{r}_{k'l'm'\sigma'})\phi_i(\boldsymbol{r}_{k'l'm'\sigma'}q) = e_i\phi_i(\boldsymbol{r}_{klm}\sigma q),$$
$$k,l,m = 1,\ldots,n, \qquad (4.19)$$

where the position vector $\boldsymbol{r}_{klm}$ represents (x_k, y_l, z_m). Since the local single-particle hamiltonian $h_q(\boldsymbol{r}\sigma\sigma')$ involves the differential operator, the discretised single-particle hamiltonian becomes the non-local matrix form. Eq. (4.19) is a result of the variational equation of the energy functional expressed in the orthogonal basis functions $f_{klm}(x,y,z)$. Thus, it provides the upper bound of the total binding energy.

4.1.3 Solution of HF equation in mesh representation

In this subsection, we explain the iterative solution of SHF equation (3.73) in the mesh representation. Usually the SHF equation in the mesh representation is solved in terms of the imaginary time step method (ITSM) [61]. The ITSM is a powerful tool for solving non-linear differential equation such as HF equation. However, it costs rather long computational time to converge a set of occupied single-particle wave functions at enough precision. In order to make the computational time short, we solve the SHF equation with the technique combining the conjugate gradient method (CGM) [62], which is the iterative method for solving the generalized eigenvalue equation, with the ITSM.

Imaginary time step method (ITSM)

First, we briefly explain the algorithm of the ITSM. The ITSM is the iterative method for solving Hartree-Fock equations

$$h|\phi_i\rangle = e_i|\phi_i\rangle, \qquad i = 1,\ldots,A, \qquad (4.20)$$

where h is the single-particle hamiltonian and e_i is the single-particle energy and $|\psi_i\rangle$ is the single-particle wave function. Note that the single-particle hamiltonian depends on the single particle wave functions, that is, Eq. (4.20) is a non-linear differential equation. Its algorithm is the followings:

1. Select the arbitrary initial occupied single particle wave functions $|\phi_i^{(0)}\rangle$, for example, like harmonic oscillator wave functions.

2. According as $n = 0, 1, \ldots$, following iteration are repeated until an appropriate convergence criterion is satisfied.

   (a) Construct the single-particle hamiltonian $h^{(n)}$ from the single-particle wave functions $|\phi_i^{(n)}\rangle$.

   (b) Generate the new single-particle wave functions defined by

$$|\psi_i^{(n+1)}\rangle = \exp\left[-\lambda h^{(n)}\right] |\phi_i^{(n)}\rangle \tag{4.21a}$$

$$\simeq \left[1 - \lambda h^{(n)}\right] |\phi_i^{(n)}\rangle, \tag{4.21b}$$

   where λ is a positive small parameter.

   (c) Since the set of obtained single-particle wave functions $|\psi_i^{(n+1)}\rangle$ is not orthogonal to each other, obtain a new set of orthonormal single-particle wave functions $|\phi_i^{(n+1)}\rangle$ from the single-particle wave functions $|\psi_i^{(n+1)}\rangle$ by means of the following Schmidt's orthogonalization method:

      i. Normalize $|\psi_1\rangle$ and obtatin $|\phi_1\rangle$.

$$|\phi_1\rangle = \frac{1}{\sqrt{\langle\psi_1|\psi_1\rangle}}|\psi_1\rangle. \tag{4.22}$$

      ii. For $i = 2, \ldots, A$, obtain $|\phi_i\rangle$.

$$|\phi_i'\rangle = |\psi_i\rangle - \sum_{j=1}^{i-1} |\phi_j\rangle \langle\phi_j|\psi_i\rangle, \tag{4.23a}$$

$$|\phi_i\rangle = \frac{1}{\sqrt{\langle\phi_i'|\phi_i'\rangle}}|\phi_i'\rangle. \tag{4.23b}$$

As a convergence criterion of ITSM, we can consider the two cases: One is the difference between the total binding energy of the $(n-1)$-th step and the ones of the n-th step:

$$\Delta E^{(n)} \equiv E^{(n-1)} - E^{(n)} \leq \epsilon_E, \tag{4.24}$$

where $E^{(n)}$ is the total energy of the n-th time step and ϵ_E is a parameter to determine the convergence criterion, e.g. $\epsilon_E = 10^{-10}$ MeV. The other is the root mean deviations of the single-particle hamiltonian for each single-particle wave function:

$$\Delta e_i^{(n)} \equiv \sqrt{\left|\langle\phi_i^{(n)}|h^{(n)2}|\phi_i^{(n)}\rangle - \langle\phi_i^{(n)}|h^{(n)}|\phi_i^{(n)}\rangle^2\right|} \leq \epsilon_e, \quad i = 1, \ldots, A, \tag{4.25}$$

where ϵ_e is a parameter to determine the convergence criterion, e.g. $\epsilon_e = 10^{-5}$ MeV. The convergence criterion with the root mean deviations of the single-particle hamiltonian in Eq. (4.25) is more strict than those with the energy difference in Eq. (4.24) because the convergence criterion with the root mean deviations of the single-particle hamiltonian assure that the all of the occupied single-particle wave functions are the eigenfunctions of the single-particle hamiltonian.

Since the RPA equations (3.73) are based on the HF ground state, it is essential that we solve the HF equations as accurately as possible. Thus, in this thesis, we use the convergence criterion of Eq. (4.25) when we solve the SHF equation (3.69).

Conjugate gradient method (CGM)

Secondly, we explain the algorithm of the CGM [62]. The CGM is the iterative method for obtaining the eigenvector with lowest eigenvalue of the generalized eigenvalue equation:

$$C\boldsymbol{x} = kD\boldsymbol{x}, \tag{4.26}$$

where the matrices C and D are hermitian and k is real eigenvalue[1]. Note that the matrices C and D are fixed as given matrices, that is, for example, Eq. (4.26) is regarded as the linear differential equation in the mesh representation. Its algorithm is the following:

1. Select the arbitrary initial vector $\boldsymbol{x}_0$ and calculate the following quantities:

$$f_0 = \frac{(\boldsymbol{x}_0, C\boldsymbol{x}_0)}{(\boldsymbol{x}_0, D\boldsymbol{x}_0)} \tag{4.27a}$$

$$\boldsymbol{g}_0 = \frac{2(C\boldsymbol{x}_0 - f_0 D\boldsymbol{x}_0)}{(\boldsymbol{x}_0, D\boldsymbol{x}_0)} \tag{4.27b}$$

$$\boldsymbol{p}_0 = -\boldsymbol{g}_0 \tag{4.27c}$$

2. According as $k = 0, 1, \ldots$, the following procedures of iteration are

[1] In the original paper [62], the C and D are real symmetric matrices. We expand the solution of eigenvalue equation with the real matrices into the one of the hermitian matrix in this subsection, where we make use of the fact that the hermitian matrix equation is rewritten into the real symmetric matrix equation with same eigenvalue. Therefore, the eigenvalue k is real.

repeated until an appropriate convergence criterion is satisfied:

$$a_k = \mathrm{Re}\left[(\boldsymbol{p}_k, C\boldsymbol{p}_k)(\boldsymbol{x}_k, D\boldsymbol{p}_k) - (\boldsymbol{x}_k, C\boldsymbol{p}_k)(\boldsymbol{p}_k, D\boldsymbol{p}_k)\right], \tag{4.28a}$$

$$b_k = \mathrm{Re}\left[(\boldsymbol{p}_k, C\boldsymbol{p}_k)(\boldsymbol{x}_k, D\boldsymbol{x}_k) - (\boldsymbol{x}_k, C\boldsymbol{x}_k)(\boldsymbol{p}_k, D\boldsymbol{p}_k)\right], \tag{4.28b}$$

$$c_k = \mathrm{Re}\left[(\boldsymbol{x}_k, C\boldsymbol{p}_k)(\boldsymbol{x}_k, D\boldsymbol{x}_k) - (\boldsymbol{x}_k, C\boldsymbol{x}_k)(\boldsymbol{x}_k, D\boldsymbol{p}_k)\right], \tag{4.28c}$$

$$\alpha_k = \frac{-b_k + \sqrt{b_k^2 - 4a_k c_k}}{2a_k}, \tag{4.28d}$$

$$\boldsymbol{x}_{k+1} = \boldsymbol{x}_k + \alpha_k \boldsymbol{p}_k, \tag{4.28e}$$

$$f_{k+1} = \frac{(\boldsymbol{x}_{k+1}, C\boldsymbol{x}_{k+1})}{(\boldsymbol{x}_{k+1}, D\boldsymbol{x}_{k+1})}, \tag{4.28f}$$

$$\boldsymbol{g}_{k+1} = \frac{2(C\boldsymbol{x}_{k+1} - f_{k+1} D\boldsymbol{x}_{k+1})}{(\boldsymbol{x}_{k+1}, D\boldsymbol{x}_{k+1})}, \tag{4.28g}$$

$$\beta_k = \frac{(\boldsymbol{g}_{k+1}, \boldsymbol{g}_{k+1})}{(\boldsymbol{g}_k, \boldsymbol{g}_k)}, \tag{4.28h}$$

$$\boldsymbol{p}_{k+1} = -\boldsymbol{g}_{k+1} + \beta_k \boldsymbol{p}_k, \tag{4.28i}$$

Note that the quantities f_{k+1} and β_k are real. And, it is demanded that the quantity α_k is real in each iteration step.

3. Combining Schmidt's orthogonalization method with the above iteration process, the eigenvectors are obtained in order of increasing eigenvalues.

The CGM can be efficiently used in order to obtain the unoccupied single-particle wave functions. Now, the occupied single-particle wave functions of the ground state and the HF hamiltonian h_{HF} are obtained already. Then, the HF equation for the unoccupied single-particle wave function is given by

$$h_{\mathrm{HF}}|\phi_m\rangle = e_m|\phi_m\rangle, \qquad m = A+1, \ldots \tag{4.29}$$

Note that Eq. (4.29) is a linear differential equation. Substituting the HF hamiltonian h_{HF} and the unit matrix for C and D in Eq. (4.20) respectively, the CGM can be applied to Eq. (4.29). Using Schmidt's orthogonalization method, an unoccupied single-particle wave function is obtained in order of increasing eigenvalue. As a convergence criterion of CGM, we use the following one:

$$\Delta e_m^{(k)} \equiv \sqrt{\left|\langle\phi_m^{(k)}|h_{\mathrm{HF}}^2|\phi_m^{(k)}\rangle - \langle\phi_m^{(k)}|h_{\mathrm{HF}}|\phi_m^{(n)}\rangle^2\right|} \leq \epsilon_e. \tag{4.30}$$

Note that the single-particle hamiltonian h_{HF} is fixed in the iteration process.

ITSM plus CGM

At the last, we explain the technique combining the CGM with the ITSM, which is used when we solve the SHF equation (3.69) for occupied single-particle wave functions in actual numerical calculation. Here, we call the technique combining the CGM with the ITSM "ITSM plus CGM".

In Fig. 4.1, we show how the convergence criterion (4.25) is satisfied in the iteration process when the SHF equation is solved. The calculations are for the 8-particle 8-hole state (superdeformed state) of ^{40}Ca. The results of the two methods, ITSM and ITSM plus CGM, are displayed in Fig. 4.1.

We can see in Fig. 4.1 that the root mean deviations $\Delta e_i^{(n)}$ with the ITSM take varied values from orbital to orbital in the iteration process, that is, the degree of convergence for each of the single-particle wave functions is different. Thus, we make use of the CGM in order to arrange root mean deviations $\Delta e_i^{(n)}$ in (4.25) into the same size.

The algorithm of ITSM plus CGM used in the actual numerical calculation is the followings:

1. Select the arbitrary initial occupied single-particle wave functions and start the ITSM.

2. According as $\lambda = 1, \ldots, 12$, initialize a parameter r into zero and repeat the following iteration until the convergence criterion defined as

$$|E^{(n-10)} - E^{(n)}| \leq 10^{-\lambda} \text{ MeV} \tag{4.31}$$

   is satisfied:

   (a) Proceed the ten iterations of ITSM. Put present number of iterations into n. Arrange the single-particle wave functions $\phi_i^{(n)}$ in order of increasing eigenvalue.

   (b) Perform the CGM if the following condition is satisfied:

$$\frac{1}{A}\sum_{i=1}^{A}\left(\Delta e_i^{(n)}\right)^2 \geq 10^r \Delta E^{(n)}, \tag{4.32}$$

   where $\Delta E^{(n)}$ is defined by Eq. (4.24) and $\Delta e_i^{(n)}$ is defined by Eq. (4.25). The procedure when CGM is performed is the followings:

      i. Put a set of the occupied single-particle wave functions $\phi_i^{(n)}$ into ψ_i.

ii. Solve the following linear differential equation by means of CGM:

$$h^{(n)}|\psi_1\rangle = \lambda_1|\psi_1\rangle \tag{4.33}$$

where $h^{(n)}$ is a fixed single-particle hamiltonian in the iteration process of CGM. The convergence criterion of CGM is given by

$$\left|\langle\psi_i|h^{(n)2}|\psi_i\rangle - \langle\psi_i|h^{(n)}|\psi_i\rangle^2\right| \leq 10^r \Delta E^{(n)}, \qquad i = 1, \ldots, A. \tag{4.34}$$

iii. Using Schmidt's orthogonalization method, obtain the subsequent eigenstate with larger eigenvalues in order of increasing eigenvalue.

iv. Put ψ_i into $\phi_i^{(n)}$.

v. Add one to the parameter r if the total binding energy rises after CGM.

Note that unit of the left-hand side in Eqs. (4.32) and (4.34) is different from the one of the right-hand side. Here, we empirically determine the condition (4.32). The parameter r is necessary to avoid divergence.

The iteration process of the ITSM is different from the one of the CGM. In one iteration of the ITSM, a set of operations of multiplying the single-particle hamiltonian on a set of the occupied single particle wave functions is needed. So, we readjust the number of iterations in the iteration process of the CGM in terms of the number of such operation in Fig. 4.1.

We can see in Fig. 4.1 that the convergence of ITSM plus CGM is about ten-times faster than the ones of the ITSM when we solve the Hartree-Fock equation (3.73) under convergence criterion (4.25).

4.1.4 Spatial symmetry of the single-particle wave function

In the case of spherical, axial and triaxial nuclei, we can impose the symmetry with respect to reflection in $x = 0$, $y = 0$ and $z = 0$-plane on the density $\rho_q(\boldsymbol{r})$ in Eq. (3.63a). In order to impose such symmetries on the density, we impose the following spatial symmetries on the single-particle wave functions $\phi_i(\boldsymbol{r}\sigma q)$ in Eq. (3.62) [26, 63]:

- Parity

$$\begin{aligned}\hat{P}\phi_i(x, y, z, \sigma, q) &= \phi_i(-x, -y, -z, \sigma, q) \\ &= p_i\phi_i(x, y, z, \sigma, q), \qquad p_i = \pm 1\end{aligned} \tag{4.35a}$$

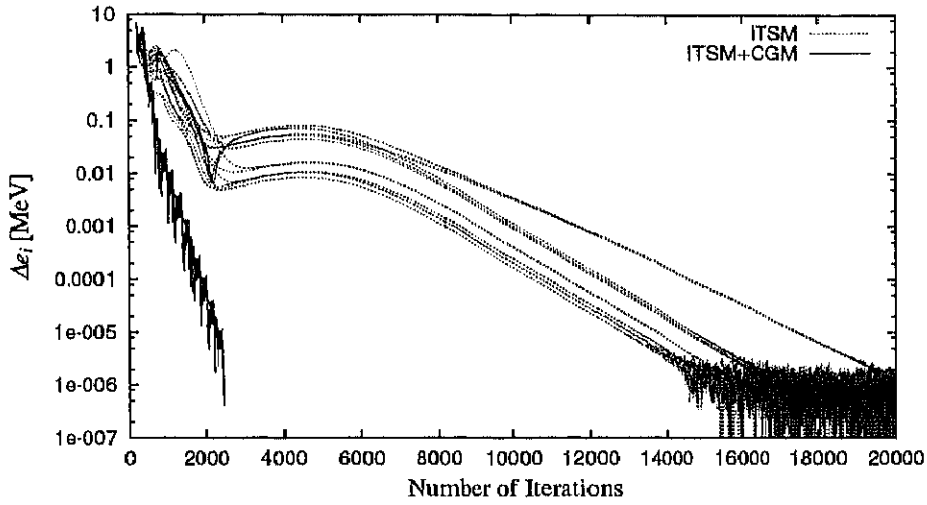

Figure 4.1: The mean square deviation of single particle hamiltonian for each of the occupied single-particle wave functions at n-th iteration, $\Delta e_i^{(n)}$, defined by Eq. (4.25). The calculation is for the 8p8h state of ^{40}Ca. "ITSM" are calculated with imaginary time step method. "ITSM+CGM" are calculated by means of the technique combined the conjugate gradient method with the imaginary time step method (see text).

- z-signature

$$\begin{aligned}\hat{R}_z\phi_i(x,y,z,\sigma,q) &= \mathrm{e}^{i\pi(\hat{J}_z-1/2)}\phi_i(x,y,z,\sigma,q)\\ &= 2\sigma\phi_i(-x,-y,z,\sigma,q)\\ &= r_i\phi_i(x,y,z,\sigma,q), \qquad r_i=1, \end{aligned} \tag{4.35b}$$

- x-T-simplex

$$\begin{aligned}\hat{S}_x^T\phi_i(x,y,z,\sigma,q) &= \hat{P}\,\mathrm{e}^{i\pi(\hat{J}_x-1/2)}\mathcal{T}\phi_i(x,y,z,\sigma,q)\\ &= 2\sigma\phi_i^*(-x,y,z,\sigma,q)\\ &= s_i\phi_i(x,y,z,\sigma,q), \qquad s_i=1, \end{aligned} \tag{4.35c}$$

Where the subscript i runs over from 1 to $A/2$. The operators $\hat{P}$, $\hat{R}_z$ and $\hat{S}_x^T$ are parity, z-signeture and x-T-simplex operator respectively, and p_i, r_i and s_i are their eigenvalues respectively. The parity, z-signature and x-T-simplex quantum numbers for the time reversed state $\phi_{\bar{i}}$ are give by

$$p_{\bar{i}} = p_i, \qquad r_{\bar{i}} = -1, \qquad s_{\bar{i}} = -1. \tag{4.36}$$

Note that z-signature and x-T-simplex operators are different from usual ones by the phase [63]. We can rewrite Eq. (4.35) into

$$\phi_i(x,y,z,\sigma,q) = 2\sigma s_i \phi_i^*(-x,y,z,\sigma,q) = 2\sigma\phi_i^*(-x,y,z,\sigma,q), \tag{4.37a}$$
$$\phi_i(x,y,z,\sigma,q) = r_i s_i \phi_i^*(x,-y,z,\sigma,q) = \phi_i^*(x,-y,z,\sigma,q), \tag{4.37b}$$
$$\phi_i(x,y,z,\sigma,q) = 2\sigma p_i r_i \phi_i(x,y,-z,\sigma,q) = 2\sigma p_i \phi_i(x,y,-z,\sigma,q). \tag{4.37c}$$

Then, we can see that the single-particle wave functions have symmetries with respect to the $x = 0$, $y = 0$ and $z = 0$ plane. Table 4.2 represents spatial symmetries of single particle wave functions defined by

$$\psi_{i,1}(\boldsymbol{r}q) = \mathrm{Re}[\phi_i(\boldsymbol{r}+q)], \tag{4.38a}$$
$$\psi_{i,2}(\boldsymbol{r}q) = \mathrm{Im}[\phi_i(\boldsymbol{r}+q)], \tag{4.38b}$$
$$\psi_{i,3}(\boldsymbol{r}q) = \mathrm{Re}[\phi_i(\boldsymbol{r}-q)], \tag{4.38c}$$
$$\psi_{i,4}(\boldsymbol{r}q) = \mathrm{Im}[\phi_i(\boldsymbol{r}-q)]. \tag{4.38d}$$

Then, we can solve the SHF equation on one eighth of the mesh space.

Table 4.2: Symmetry properties of components of single particle wave function ψ_i in Eq. (4.38) with respect to the $x = 0$, $y = 0$, and $z = 0$ plane.

	x	y	z
$\psi_{i,1}$	+	+	$+p_i$
$\psi_{i,2}$	−	−	$+p_i$
$\psi_{i,3}$	−	+	$-p_i$
$\psi_{i,4}$	+	−	$-p_i$

4.1.5 Calculation of the Coulomb potential

The Coulomb potential is necessary for the SHF calculation and used in the single-particle hamiltonian. The Coulomb potential in Eq. (3.7) is solved in terms of the conjugate gradient method (CGM) [24]. The CGM used in this subsection is the iterative method for solving a inhomogeneous linear equations and different form the CGM used when the HF equation is solved.

The Coulomb potential in Eq. (3.7) is given by

$$\Phi(\boldsymbol{r}) = e\int \mathrm{d}\boldsymbol{r}' \frac{\rho_{\mathrm{p}}(\boldsymbol{r}')}{|\boldsymbol{r}-\boldsymbol{r}'|}. \tag{4.39}$$

The Coulomb potential is the solution of the Poisson equation:

$$\triangle\Phi(\boldsymbol{r}) = -4\pi e\rho_{\rm p}(\boldsymbol{r}) \tag{4.40}$$

We discretise the Poisson equation on the 3D Cartesian mesh and approximate the Laplacian operator in terms of 9-point formula with finite difference method[2]. We solve the Poisson equation in the mesh representation by means of the CGM in order to obtain the Coulomb potential. Then, we must consider the boundary condition because the Coulomb force is a long range force.

CGM for solving the inhomogeneous linear equations

Here, we explain the CGM for solving the inhomogeneous linear equations:

$$A\boldsymbol{x} = \boldsymbol{b}, \tag{4.41}$$

where A is positive definite symmetric matrix of order n, and $\boldsymbol{x}$ and $\boldsymbol{b}$ are vectors of order n. Its algorithm is the following:

1. Select the arbitrary initial vector $\boldsymbol{x}_0$.

$$\boldsymbol{r}_0 = \boldsymbol{b} - A\boldsymbol{x}_0 \tag{4.42a}$$
$$\boldsymbol{p}_0 = \boldsymbol{r}_0 \tag{4.42b}$$

2. According as $k = 0, 1, \ldots$, following iterations are repeated until the appropriate convergence criterion is satisfied:

$$\alpha_k = \frac{(\boldsymbol{p}_k, \boldsymbol{r}_k)}{(\boldsymbol{p}_k, A\boldsymbol{p}_k)} \tag{4.43a}$$
$$\boldsymbol{x}_{k+1} = \boldsymbol{x}_k + \alpha_k \boldsymbol{p}_k \tag{4.43b}$$
$$\boldsymbol{r}_{k+1} = \boldsymbol{r}_k - \alpha_k A\boldsymbol{p}_k \tag{4.43c}$$
$$\text{If } \frac{|\boldsymbol{r}_{k+1}|}{|\boldsymbol{b}|} \leq \varepsilon, \text{ then iteration is finished.} \tag{4.43d}$$
$$\beta_k = \frac{(\boldsymbol{r}_{k+1}, \boldsymbol{r}_{k+1})}{(\boldsymbol{r}_k, \boldsymbol{r}_k)} \tag{4.43e}$$
$$\boldsymbol{p}_{k+1} = \boldsymbol{r}_{k+1} + \beta_k \boldsymbol{p}_k \tag{4.43f}$$

[2]We do not use the approximated form of differential operator with Lagrange mesh method in Eq. (4.18).

Boundary condition

Performing a multipole expansion of the Coulomb potential, we calculate the Coulomb potential over the box. Substituting the Coulomb potential over the box for Eq. (4.40), we estimate the contribution of the Coulomb potential over the box to the proton density in the box. We subtract this contribution from the proton density in the box. We consider the boundary condition in terms of such technique. Then, we solve the Poisson equation by means of the CGM.

The multipole expansion of the Coulomb potential is given by

$$\Phi(\boldsymbol{r}) = e\sum_{l=0}^{\infty}\frac{1}{r^{2l+1}}\frac{4\pi}{2l+1}\sum_{m=-l}^{l} r^l Y_{lm}(\hat{r})\int \mathrm{d}\boldsymbol{r}'\rho_{\mathrm{p}}(\boldsymbol{r}')r'^l Y^*_{lm}(\hat{r}'), \tag{4.44}$$

where $r > r'$. In actual numerical calculation, we expand until $l = 4$. We change the spherical harmonics Y_{lm} into the following ones:

$$\widetilde{Y}_{lm} = \sqrt{\frac{4\pi}{2l+1}}Y_{lm} \qquad (m = 0) \tag{4.45a}$$

$$\widetilde{Y}_{l|m|} = \sqrt{\frac{4\pi}{2l+1}}\frac{i^m}{\sqrt{2}}[Y_{l|m|} + Y_{l-|m|}] \qquad (m \neq 0) \tag{4.45b}$$

$$\widetilde{Y}_{l-|m|} = \sqrt{\frac{4\pi}{2l+1}}\frac{i^{m+1}}{\sqrt{2}}[Y_{l|m|} - Y_{l-|m|}] \qquad (m \neq 0) \tag{4.45c}$$

Then, the $r^l\widetilde{Y}_{lm}$ are given by

$$\widetilde{Y}_{00} = 1$$

$$r\widetilde{Y}_{10} = z, \qquad r\widetilde{Y}_{1-1} = x,$$

$$r\widetilde{Y}_{11} = y,$$

$$r^2\widetilde{Y}_{20} = \frac{1}{2}(3z^2 - r^2),$$

$$r^2\widetilde{Y}_{21} = \sqrt{3}yz, \qquad r^2\widetilde{Y}_{2-1} = \sqrt{3}zx,$$

$$r^2\widetilde{Y}_{22} = \frac{\sqrt{3}}{2}(y^2 - x^2), \qquad r^2\widetilde{Y}_{2-2} = \sqrt{3}xy,$$

$$r^3\widetilde{Y}_{30} = \sqrt{\frac{1}{4}}z(5z^2 - 3r^2),$$

$$r^3\widetilde{Y}_{31} = \sqrt{\frac{3}{8}}y(5z^2 - r^2), \qquad r^3\widetilde{Y}_{3-1} = \sqrt{\frac{3}{8}}x(5z^2 - r^2),$$

$$r^3\widetilde{Y}_{32} = \frac{\sqrt{15}}{2}z(y^2 - x^2), \qquad r^3\widetilde{Y}_{3-2} = \sqrt{15}xyz,$$

$$r^3\widetilde{Y}_{33} = \sqrt{\frac{5}{8}}y(y^2 - 3x^2), \qquad r^3\widetilde{Y}_{3-3} = \sqrt{\frac{5}{8}}x(3y^2 - x^2),$$

$$r^4\widetilde{Y}_{40} = \frac{1}{8}(35z^4 - 30r^2z^2 + 3r^4),$$

$$r^4\widetilde{Y}_{41} = \sqrt{\frac{5}{8}}(7z^2 - 3r^2)yz, \qquad r^4\widetilde{Y}_{4-1} = \sqrt{\frac{5}{8}}(7z^2 - 3r^2)zx,$$

$$r^4\widetilde{Y}_{42} = \frac{\sqrt{5}}{4}(y^2 - x^2)(7z^2 - r^2), \qquad r^4\widetilde{Y}_{4-2} = \frac{\sqrt{5}}{2}(7z^2 - r^2)xy,$$

$$r^4\widetilde{Y}_{43} = \sqrt{\frac{35}{8}}(y^2 - 3x^2)yz, \qquad r^4\widetilde{Y}_{4-3} = \sqrt{\frac{35}{8}}(3y^2 - x^2)zx,$$

$$r^4\widetilde{Y}_{44} = \frac{\sqrt{35}}{8}(x^4 - 6x^2y^2 + y^4), \qquad r^4\widetilde{Y}_{4-4} = \frac{\sqrt{35}}{2}(y^2 - x^2)xy.$$

In terms of $r^l\widetilde{Y}_{lm}$, the multipole expansion of the Coulomb potential in Eq. (4.42) is given by

$$\Phi(\boldsymbol{r}) = \frac{e}{4\pi\epsilon_0}\sum_{l=0}^{\infty}\frac{1}{r^{2l+1}}\sum_{m=-l}^{l} r^l\widetilde{Y}_{lm}(\hat{r})\int \mathrm{d}\boldsymbol{r}'\rho_{\mathrm{p}}(\boldsymbol{r}')r'^l\widetilde{Y}_{lm}(\hat{r}'). \tag{4.46}$$

For triaxial nuclei, it is necessary to include only the following components in the multipole expansion up to $l = 4$:

$$\widetilde{Y}_{00}, \quad r^2\widetilde{Y}_{20}, \quad r^2\widetilde{Y}_{22}, \quad r^4\widetilde{Y}_{40}, \quad r^4\widetilde{Y}_{42}, \quad r^4\widetilde{Y}_{44}. \tag{4.47}$$

4.1.6 Deformation parameter

The mass-quadrupole moments is given as

$$\alpha_{2m} = \sqrt{\frac{4\pi}{5}} \frac{\int \widetilde{Y}_{2m}(\boldsymbol{r})\rho(\boldsymbol{r})\mathrm{d}\boldsymbol{r}}{\int r^2\rho(\boldsymbol{r})\mathrm{d}\boldsymbol{r}}, \qquad m = -2, \ldots, 2. \tag{4.48}$$

Then, β and γ-deformation parameter is defined as

$$\alpha_{20} = \beta\cos\gamma, \qquad \alpha_{22} = \beta\sin\gamma. \tag{4.49}$$

4.2 RPA calculation in the mesh representation

In this section, we explain the techniques employed in solving the RPA equation in the mesh representation. The RPA equations (3.72) for the time-reversal pair of the RPA wave functions in Eq. (3.64) are made of the single-particle wave functions in Eq. (3.62), which are obtained in the SHF calculation in section 4.1. The RPA equation is solved for one member of the pair.

In subsection 4.2.1, we explain the iterative solution of RPA equation in the mesh representation. In subsection 4.2.2, we explain how we impose the spatial symmetry on the single-particle wave functions and introduce the quantum number related with the spatial symmetry. In subsection 4.2.3, we explain the excited state with quantum number introduced in subsection 4.2.2.

4.2.1 Solution of RPA equation in mesh representation

First, in this subsection, we explain the solution method of the RPA equation (2.34) for the RPA wave functions $X_i^\lambda(x)$ and $Y_i^\lambda(x)$ in the mesh representation, which is explained in Ref. [29]. Secondly, we also explain the solution method of the RPA equations (2.47) for the RPA wave functions $\phi_i^{(\pm)\lambda}(x)$ in the mesh representation. At the end of this subsection, we explain how we use the above two solution methods in the actual numerical calculation.

We briefly rewrite Eq. (2.34) in the mesh representation as the matrix form

$$S\boldsymbol{X}^\lambda = \hbar\omega_\lambda I\boldsymbol{X}^\lambda \tag{4.50}$$

where

$$S = \begin{pmatrix} A & B \\ B^* & A^* \end{pmatrix}, \tag{4.51a}$$

$$I = \begin{pmatrix} 1 & 0 \\ 0 & -1 \end{pmatrix}, \tag{4.51b}$$

$$\boldsymbol{X}^\lambda = \begin{pmatrix} X \\ Y \end{pmatrix}_\lambda . \tag{4.51c}$$

And we also rewrite Eq. (2.47) in the mesh representation as the matrix form

$$S\boldsymbol{\phi}^{(+)\lambda} = \hbar\frac{\omega_\lambda^2}{|\omega_\lambda|}\boldsymbol{\phi}^{(-)\lambda}, \tag{4.52a}$$

$$T\boldsymbol{\phi}^{(-)\lambda} = \hbar|\omega_\lambda|\boldsymbol{\phi}^{(+)\lambda}, \tag{4.52b}$$

where

$$T = ISI\begin{pmatrix} A & -B \\ -B^* & A^* \end{pmatrix}, \tag{4.53a}$$

$$\boldsymbol{\phi}^{(+)\lambda} = \begin{pmatrix} \phi^{(+)} \\ \phi^{(+)*} \end{pmatrix}_\lambda , \tag{4.53b}$$

$$\boldsymbol{\phi}^{(-)\lambda} = \begin{pmatrix} \phi^{(-)} \\ \phi^{(-)*} \end{pmatrix}_\lambda . \tag{4.53c}$$

If $\hbar\omega_\lambda > 0$, then Eqs. (4.52) are written as

$$S\boldsymbol{\phi}^{(+)\lambda} = \hbar\omega_\lambda\boldsymbol{\phi}^{(-)\lambda}, \tag{4.54a}$$

$$T\boldsymbol{\phi}^{(-)\lambda} = \hbar\omega_\lambda\boldsymbol{\phi}^{(+)\lambda}. \tag{4.54b}$$

Solution of RPA equation for the wave functions $X_i^\lambda(x)$ and $Y_i^\lambda(x)$

According to Ref. [29], we can solve the RPA equation by means of the CGM, which is explained in the subsection 4.1.3.[3] Eq. (4.50) satisfies the necessary condition for applying the CGM: The matrices in both sides of Eq. (4.50), S and I, are hermitian. Then, we can obtain the RPA wave functions $X_i^\lambda(x)$ and $Y_i^\lambda(x)$ with the lowest real eigenvalue $\hbar\omega_\lambda$ by means of the CGM. Making use of the Schmidt orthogonalization method, we can obtain the solutions in order of increasing eigenvalue.

[3]The algorithm of CGM used in our thesis is somewhat different from the ones in Ref. [29]

One might wonder why the lowest eigenvalue of the RPA equation is not negative. The reason is that the norm of the eigenvector of Eq. (4.50) is fixed to 1 in iteration process of the CGM. Remember that the eigenvalues with positive (negative) norm is positive (negative) (see section 2.1.1).

There always exist the translational spurious solutions with the zero-eigenvalues of the RPA equation and the rotational spurious solutions of the RPA equation for the deformed nuclei. It is well known that the norm of the spurious state with the RPA amplitude X^{λ}_{mi} and Y^{λ}_{mi} is vanishing, that is, the one with the RPA wave functions $X^{\lambda}_{i}(x)$ and $Y^{\lambda}_{i}(x)$ is vanishing. However, in actual numerical calculation, the eigenvalues of the spurious states are almost never vanishing because of truncation in the calculation and numerical errors. Such eigenvalues are not so small in 3D Cartesian mesh calculation (see section 4.3). Therefore, we can numerically treat the spurious state as the one with non-vanishing eigenvalue. All of the eigenvalues of the computational spurious states should be real if the HF equation is solved without constraint and symmetry restriction [49]. This is just the reason we can solve Eq. (4.50) for the RPA wave function $X^{\lambda}_{i}(x)$ and $Y^{\lambda}_{i}(x)$ by means of the CGM and can obtain the spurious states with non-zero eigenvalue.

Solution of RPA equations for the wave functions $\phi^{(\pm)\lambda}_{i}(x)$

If the HF equation is solved with constraint or symmetry restriction, then the eigenvalues of the computational spurious state are not always real. There is possibility of pure imaginary eigenvalue. On that occasion, we can no longer use the CGM in solving Eq. (4.50) because one of the condition to use CGM that all of the eigenvalues are real is not satisfied. In actual numerical calculation, the constraint or symmetry restriction is usually imposed. Therefore, we develop the method for calculating the computational spurious state with the pure imaginary eigenvalue.

The norm of the RPA amplitude X^{λ}_{mi} and Y^{λ}_{mi} with the pure imaginary eigenvalue is vanishing (see subsection 2.1.3). Therefore, the RPA equations (4.52) for the wave functions $\phi^{(\pm)\lambda}_{i}$ is more appropriate for handling the pure imaginary eigenvalue. In order to apply CGM, we rewrite Eqs. (4.52) into the single equation for the RPA wave function $\phi^{(-)}$

$$ST\phi^{(-)\lambda} = (\hbar\omega_{\lambda})^2\phi^{(-)\lambda}. \tag{4.55}$$

The eigenvalue $(\hbar\omega_{\lambda})^2$ of Eq. (4.55) is real even though $\hbar\omega_{\lambda}$ is pure imaginary. Acting the matrix T of Eq. (4.53a) on both sides of Eq. (4.55), we obtain the following equation:

$$TST\phi^{(-)\lambda} = (\hbar\omega_{\lambda})^2 T\phi^{(-)\lambda}. \tag{4.56}$$

Eq. (4.56) satisfies the necessary condition for applying the CGM: The matrices in both sides of Eq. (4.56), TST and T, are hermitian. Then, we obtain the RPA wave function $\phi_i^{(-)\lambda}$ with lowest eigenvalue $(\hbar\omega_\lambda)^2$ by means of CGM. Putting the RPA wave function $\phi_i^{(-)\lambda}$ and the root of absolute eigenvalue $\hbar|\omega_\lambda|$ into Eq. (4.52b), the RPA wave function $\phi_i^{(+)\lambda}(x)$ is obtained. If the eigenvalue of Eq. (4.56), $(\hbar\omega_\lambda)^2$, is negative, the eigenvalue of the RPA equation, $\hbar\omega_\lambda$, is pure imaginary. Using the Schmidt orthogonalization method, we can obtain the eigenstates in order of increasing eigenvalue $(\hbar\omega_\lambda)^2$. Incidentally, even if the eigenvalue of computational spurious state is vanishing, we can solve the Eq. (4.56) by the CGM just as in the case where the eigenvalue is not vanishing.

In actual numerical calculation, we do not just apply the CGM to Eq. (4.56) in order to accelerate convergence. We assume that the matrix T is positive definite. Then, Eq. (4.56) is changed into

$$R\boldsymbol{y} = k\boldsymbol{y}, \tag{4.57}$$

where

$$R = \sqrt{T}S\sqrt{T}, \qquad \boldsymbol{y} = \sqrt{T}\boldsymbol{x}, \qquad \boldsymbol{x} = \boldsymbol{\phi}^{(-)\lambda}, \qquad k = (\hbar\omega_\lambda)^2. \tag{4.58}$$

Thus, we can apply the CGM to Eq. (4.57). Using S, T and $\boldsymbol{x} = \boldsymbol{\phi}^{(-)\lambda}$, the algorithm of CGM is modified into the following one:

1. Select the arbitrary initial vector $\boldsymbol{x}_0$.

$$f_0 = \frac{(T\boldsymbol{x}_0, ST\boldsymbol{x}_0)}{(T\boldsymbol{x}_0, \boldsymbol{x}_0)} \tag{4.59a}$$

$$\boldsymbol{g}_0 = \frac{2(ST\boldsymbol{x}_0 - f_0\boldsymbol{x}_0)}{(T\boldsymbol{x}_0, \boldsymbol{x}_0)} \tag{4.59b}$$

$$\boldsymbol{p}_0 = -\boldsymbol{g}_0 \tag{4.59c}$$

2. Starting with $k = 0$, the following iteration procedures for $k = 1, 2, \ldots$

are repeated until convergence criterion is satisfied.

$$a_k = \mathrm{Re}\left[(T\boldsymbol{p}_k, ST\boldsymbol{p}_k)(T\boldsymbol{x}_k, \boldsymbol{p}_k) - (T\boldsymbol{x}_k, ST\boldsymbol{p}_k)(T\boldsymbol{p}_k, \boldsymbol{p}_k)\right] \quad (4.60a)$$

$$b_k = \mathrm{Re}\left[(T\boldsymbol{p}_k, ST\boldsymbol{p}_k)(T\boldsymbol{x}_k, \boldsymbol{x}_k) - (T\boldsymbol{x}_k, ST\boldsymbol{x}_k)(T\boldsymbol{p}_k, \boldsymbol{p}_k)\right] \quad (4.60b)$$

$$c_k = \mathrm{Re}\left[(T\boldsymbol{x}_k, ST\boldsymbol{p}_k)(T\boldsymbol{x}_k, \boldsymbol{x}_k) - (T\boldsymbol{x}_k, ST\boldsymbol{x}_k)(T\boldsymbol{x}_k, \boldsymbol{p}_k)\right] \quad (4.60c)$$

$$\alpha_k = \frac{-b_k + \sqrt{b_k^2 - 4a_k c_k}}{2a_k} \quad (4.60d)$$

$$\boldsymbol{x}_{k+1} = \boldsymbol{x}_k + \alpha_k \boldsymbol{p}_k \quad (4.60e)$$

$$f_{k+1} = \frac{(T\boldsymbol{x}_{k+1}, ST\boldsymbol{x}_{k+1})}{(T\boldsymbol{x}_{k+1}, \boldsymbol{x}_{k+1})} \quad (4.60f)$$

$$\boldsymbol{g}_{k+1} = \frac{2(ST\boldsymbol{x}_{k+1} - f_{k+1}\boldsymbol{x}_{k+1})}{(T\boldsymbol{x}_{k+1}, \boldsymbol{x}_{k+1})} \quad (4.60g)$$

$$\beta_k = \frac{(T\boldsymbol{g}_{k+1}, \boldsymbol{g}_{k+1})}{(T\boldsymbol{g}_k, \boldsymbol{g}_k)} \quad (4.60h)$$

$$\boldsymbol{p}_{k+1} = -\boldsymbol{g}_{k+1} + \beta_k \boldsymbol{p}_k \quad (4.60i)$$

A quantity renewed with above algorithm is $\phi^{(-)\lambda}$. So, we can regard the above algorithm as iterative solution of Eq. (4.56).

Procedure of actual numerical calculation

For actual numerical calculation, we solve Eq. (4.56) for spurious state and Eq. (4.50) for physical states in order to accelerate convergence. Then, it is necessary to orthonormalize the RPA wave functions $X_i^\lambda(x)$ and $Y_i^\lambda(x)$ in terms of the RPA wave functions $\phi_i^{(\pm)}(x)$. So, the wave function $\phi_i^{(\pm)}(x)$ must be changed into $X_i^\lambda(x)$ and $Y_i^\lambda(x)$

$$X_i^\lambda(x) = \frac{1}{2}\left[\phi_i^{(+)\lambda}(x) + \phi_i^{(-)\lambda}(x)\right], \quad (4.61a)$$

$$Y_i^\lambda(x) = \frac{1}{2}\left[\phi_i^{(+)\lambda *}(x) - \phi_i^{(-)\lambda *}(x)\right]. \quad (4.61b)$$

Here, we assume that all of the eigenvalues of computational spurious states are non-vanishing. Then, we can apply the Schmidt orthonormalization method to the RPA wave functions $X_i^\lambda(x)$ and $Y_i^\lambda(x)$ with higher excitation energy in terms of not only the orthonormalization relations in Eq. (2.39a) but also those in Eq. (2.39b)

In our computational code, we calculate Eq. (3.73) instead of Eq. (2.34) or Eq. (2.47). It is because we just use the HF computational code in several parts of RPA calculation and make use of the time-reversal properties. In

the case of the calculation of spurious state, we directly calculate Eq. (3.73) instead of Eq. (2.47). In the case of the calculation of physical state, we make use of the following relation:

$$S\boldsymbol{X}^{\lambda} = S\boldsymbol{\phi}^{(+)\lambda} + IT\boldsymbol{\phi}^{(-)\lambda} \tag{4.62}$$

We change the RPA wave functions $X_i^{\lambda}(x)$ and $Y_i^{\lambda}(x)$ into the RPA wave functions $\phi_i^{(\pm)\lambda}(x)$. Then, we calculate the first term and the second term of the right-hand side of Eq. (4.62) in terms of Eq. (3.73) respectively. Adding the first term and the second term, we obtain the quantity $S\boldsymbol{X}^{\lambda}$ in the left-hand side of Eq. (4.62).

In the case of the calculation of the spurious state, we use the following convergence criterion:

$$\{(\hbar\omega_{\lambda})^2\}^{(n-1)} - \{(\hbar\omega_{\lambda})^2\}^{(n)} \leq 10^{-10}\ \mathrm{MeV}^2, \tag{4.63}$$

where the label (n) represent the number of the iteration. In the case of the calculation of the physical state, we use the following convergence criterion:

$$\hbar\omega_{\lambda}^{(n-1)} - \hbar\omega_{\lambda}^{(n)} \leq 10^{-10}\ \mathrm{MeV}. \tag{4.64}$$

4.2.2 Spatial symmetry

In subsection 4.1.4, we imposed the symmetry with respect to reflection in $x = 0$, $y = 0$ and $z = 0$-plane on the density $\rho_q(\boldsymbol{r})$ in Eq. (3.63a). Then, we can impose the same symmetries on the transition density $\rho_q^{(+)\lambda}(\boldsymbol{r})$ in Eq. (3.65a). In order to impose such symmetries on the transition density, we impose the following spatial symmetries on the RPA wave functions $\phi_i^{(\pm)\lambda}(\boldsymbol{r}\sigma q)$ in Eq. (3.64):

- Parity

$$\begin{aligned}\hat{P}\phi_i^{(\pm)\lambda}(x,y,z,\sigma,q) &= \phi_i^{(\pm)\lambda}(-x,-y,-z,\sigma,q) \\ &= p_i{}^{\lambda}\phi_i^{(\pm)\lambda}(x,y,z,\sigma,q), \qquad p_i{}^{\lambda} = p^{\lambda}/p_i,\end{aligned} \tag{4.65a}$$

- z-signature

$$\begin{aligned}\hat{R}_z\phi_i^{(\pm)\lambda}(x,y,z,\sigma,q) &= 2\sigma\phi_i^{(\pm)\lambda}(-x,-y,z,\sigma,q) \\ &= r_i{}^{\lambda}\phi_i^{(\pm)\lambda}(x,y,z,\sigma,q), \qquad r_i{}^{\lambda} = r^{\lambda}/r_i = r^{\lambda},\end{aligned} \tag{4.65b}$$

- x-T-simplex

$$\hat{S}_x^T \phi_i^{(\pm)\lambda}(x,y,z,\sigma,q) = 2\sigma \phi_i^{(\pm)\lambda *}(-x,y,z,\sigma,q) \\ = s_i{}^\lambda \phi_i^{(\pm)\lambda}(x,y,z,\sigma,q), \qquad s_i{}^\lambda = s^\lambda / s_i = s^\lambda, \tag{4.65c}$$

where the subscript i runs over from 1 to $A/2$. The values of parameters p^λ, r^λ and s^λ are given by

$$p^\lambda = \pm 1, \qquad r^\lambda = \pm 1, \qquad s^\lambda = \pm 1. \tag{4.66}$$

The parameters p^λ, r^λ and s^λ determine the spatial symmetry of the transition density, that is, the parameters is considered as the quantum number. We classify the excited state into eight groups in terms of the parameters $(p^\lambda, r^\lambda, s^\lambda)$.

We define the simplex operator $\hat{S}_k$ as

$$\hat{S}_x \rho^{(+)\lambda}(x,y,z)\hat{S}_x^\dagger = \rho^{(+)\lambda}(-x,y,z) = s_x^\lambda \rho^{(+)\lambda}(x,y,z), \tag{4.67a}$$
$$\hat{S}_y \rho^{(+)\lambda}(x,y,z)\hat{S}_y^\dagger = \rho^{(+)\lambda}(x,-y,z) = s_y^\lambda \rho^{(+)\lambda}(x,y,z), \tag{4.67b}$$
$$\hat{S}_z \rho^{(+)\lambda}(x,y,z)\hat{S}_z^\dagger = \rho^{(+)\lambda}(x,y,-z) = s_z^\lambda \rho^{(+)\lambda}(x,y,z), \tag{4.67c}$$

where the parameters (s_x, s_y, s_z) are given by

$$s_x^\lambda = s^\lambda, \qquad s_y^\lambda = r^\lambda s^\lambda, \qquad s_z^\lambda = p^\lambda r^\lambda. \tag{4.68}$$

So, the parameters (s_x, s_y, s_z) are also quantum numbers. We can use the quantum number (s_x, s_y, s_z) instead of the quantum number $(p^\lambda, r^\lambda, s^\lambda)$. Table 4.3 represents spatial symmetries of RPA single particle wave functions defined by

$$\psi_{i,1}^{(\pm)\lambda}(rq) = \mathrm{Re}[\phi_i^{(\pm)\lambda}(r+q)], \tag{4.69a}$$
$$\psi_{i,2}^{(\pm)\lambda}(rq) = \mathrm{Im}[\phi_i^{(\pm)\lambda}(r+q)], \tag{4.69b}$$
$$\psi_{i,3}^{(\pm)\lambda}(rq) = \mathrm{Re}[\phi_i^{(\pm)\lambda}(r-q)], \tag{4.69c}$$
$$\psi_{i,4}^{(\pm)\lambda}(rq) = \mathrm{Im}[\phi_i^{(\pm)\lambda}(r-q)]. \tag{4.69d}$$

Then, we can solve the RPA equation in one eighth of the mesh space.

4.2.3 Quantum number

In the previous subsection, we classified the excited state under the quantum number $(s_x^\lambda, s_y^\lambda, s_z^\lambda)$ or $(p^\lambda, r^\lambda, s^\lambda)$. Then, we can calculate each state

Table 4.3: Symmetry properties of the $\psi_i^{(\pm)\lambda}$ with respect to the $x=0, y=0$, and $z=0$ plane in the case of $p_i=1$, where p_i is the parity of single-particle wave function $\phi_i(r\sigma q)$. In the case of $p_i=-1$, all of the signs of the column of z are changed into the opposite ones.

$(p^\lambda, r^\lambda, s^\lambda)$	$(+,+,+)$	$(+,-,+)$	$(+,-,-)$	$(+,+,-)$
$(s_x^\lambda, s_y^\lambda, s_z^\lambda)$	$(+,+,+)$	$(+,-,-)$	$(-,+,-)$	$(-,-,+)$
	$x\ y\ z$	$x\ y\ z$	$x\ y\ z$	$x\ y\ z$
$\psi_{i,1}^{(\pm)\lambda}$	$+\ +\ +$	$+\ -\ -$	$-\ +\ -$	$-\ -\ +$
$\psi_{i,2}^{(\pm)\lambda}$	$-\ -\ +$	$-\ +\ -$	$+\ -\ -$	$+\ +\ +$
$\psi_{i,3}^{(\pm)\lambda}$	$-\ +\ -$	$-\ -\ +$	$+\ +\ +$	$+\ -\ -$
$\psi_{i,4}^{(\pm)\lambda}$	$+\ -\ -$	$+\ +\ +$	$-\ -\ +$	$-\ +\ -$
$(p^\lambda, r^\lambda, s^\lambda)$	$(-,+,-)$	$(-,-,-)$	$(-,-,+)$	$(-,+,+)$
$(s_x^\lambda, s_y^\lambda, s_z^\lambda)$	$(-,-,-)$	$(-,+,+)$	$(+,-,+)$	$(+,+,-)$
	$x\ y\ z$	$x\ y\ z$	$x\ y\ z$	$x\ y\ z$
$\psi_{i,1}^{(\pm)\lambda}$	$-\ -\ -$	$-\ +\ +$	$+\ -\ +$	$+\ +\ -$
$\psi_{i,2}^{(\pm)\lambda}$	$+\ +\ -$	$+\ -\ +$	$-\ +\ +$	$-\ -\ -$
$\psi_{i,3}^{(\pm)\lambda}$	$+\ -\ +$	$+\ +\ -$	$-\ -\ -$	$-\ +\ +$
$\psi_{i,4}^{(\pm)\lambda}$	$-\ +\ +$	$-\ -\ -$	$+\ +\ -$	$+\ -\ +$

independently. It enable us to calculate the stable excited states other than unstable states. (See section 6.2.) In this subsection, We consider the case of a state with quantum number $(s_x^\lambda, s_y^\lambda, s_z^\lambda)$. If there exists no spurious state for the given quantum number, we solve the RPA equation (4.50) from the beginning. The transition Coulomb potential in Eq. (3.66) is calculated with the CGM in subsection 4.1.5.

- $(s_x^\lambda, s_y^\lambda, s_z^\lambda) = (-,+,+)$
  - There exists a spurious state of the translation for x-direction.
  - The following modified spherical harmonics in Eq. (4.45) are used in the calculation of multipole expansion of the transition Coulomb potential and the reduced transition probability of the natural parity state.

$$r\widetilde{Y}_{1,-1}, \qquad r^3\widetilde{Y}_{3,-1}, \qquad r^3\widetilde{Y}_{3,-3}.$$

- $(s_x^\lambda, s_y^\lambda, s_z^\lambda) = (+,-,+)$

- There exists a spurious state of the translation for y-direction.
- The following modified spherical harmonics are used in the calculation of multipole expansion of the transition Coulomb potential and the reduced transition probability of the natural parity state.

$$r\widetilde{Y}_{\mathbf{1,1}}, \qquad r^3\widetilde{Y}_{3,1}, \qquad r^3\widetilde{Y}_{3,3}.$$

- $(s_x^\lambda, s_y^\lambda, s_z^\lambda) = (+,+,-)$
  - There exists a spurious state of the translation for z-direction.
  - The following modified spherical harmonics are used in the calculation of multipole expansion of the transition Coulomb potential and the reduced transition probability of the natural parity state.

$$r\widetilde{Y}_{\mathbf{1,0}}, \qquad r^3\widetilde{Y}_{3,0}, \qquad r^3\widetilde{Y}_{3,2}.$$

- $(s_x^\lambda, s_y^\lambda, s_z^\lambda) = (-,-,-)$
  - There exists no spurious state.
  - The following modified spherical harmonics is used in the calculation of multipole expansion of the transition Coulomb potential and the reduced transition probability of the natural parity state.

$$r^3\widetilde{Y}_{3,-2}$$

- $(s_x^\lambda, s_y^\lambda, s_z^\lambda) = (+,-,-)$
  - There exists a spurious state of the rotation around x-axis when the nucleus is the non-axial symmetric shape around x-axis.
  - The following modified spherical harmonics are used in the calculation of multipole expansion of the transition Coulomb potential and the reduced transition probability of the natural parity state.

$$r^2\widetilde{Y}_{2,1}, \qquad r^4\widetilde{Y}_{\mathbf{4,1}}, \qquad r^4\widetilde{Y}_{4,3}.$$

- $(s_x^\lambda, s_y^\lambda, s_z^\lambda) = (-,+,-)$
  - There exists a spurious state of the rotation around y-axis when the nucleus is the non-axial symmetric shape around y-axis.
  - The following modified spherical harmonics are used in the calculation of multipole expansion of the transition Coulomb potential and the reduced transition probability of the natural parity state.

$$r^2\widetilde{Y}_{2,-1}, \qquad r^4\widetilde{Y}_{4,-1}, \qquad r^4\widetilde{Y}_{4,-3}.$$

- $(s_x^\lambda, s_y^\lambda, s_z^\lambda) = (-,-,+)$
  - There exists a spurious state of the rotation around z-axis when the nucleus is the non-axial symmetric shape around z-axis.
  - The following modified spherical harmonics are used in the calculation of multipole expansion of the transition Coulomb potential and the reduced transition probability of the natural parity state.

$$r^2\widetilde{Y}_{2,-2}, \qquad r^4\widetilde{Y}_{4,-2}, \qquad r^4\widetilde{Y}_{4,-4}.$$

- $(s_x^\lambda, s_y^\lambda, s_z^\lambda) = (+,+,+)$
  - There exists no spurious state.
  - The following modified spherical harmonics are used in the calculation of multipole expansion of the transition Coulomb potential and the reduced transition probability of the natural parity state.

$$r^0\widetilde{Y}_{0,0}, \qquad r^2\widetilde{Y}_{2,0}, \qquad r^4\widetilde{Y}_{4,0}, \qquad r^4\widetilde{Y}_{4,2}, \qquad r^4\widetilde{Y}_{4,4}.$$

The Table 4.4 shows the lowest three excitation energies with each quantum number $(s_x^\lambda, s_y^\lambda, s_z^\lambda)$ for odd parity state of ^{16}O. The employed interaction is SIII. The three excitation energies, $\hbar\omega_1$ of $(-,+,+)$, $(+,-,+)$ and $(+,+,-)$, are those of the spurious states and are pure imaginary in this calculation. The seven excitation energies, $\hbar\omega_2$ of $(-,+,+)$, $(+,-,+)$ and $(+,+,-)$, and $\hbar\omega_3$ of $(-,+,+)$, $(+,-,+)$ and $(+,+,-)$ and $\hbar\omega_1$ of $(-,-,-)$, are those of the 3_1^- state. The two excitation energies, $\hbar\omega_2$ of $(-,-,-)$ and $\hbar\omega_3$ of $(-,-,-)$ are those of the 2_1^- state. We can see that in the case of $(-,+,+)$, $(+,-,+)$ and $(+,+,-)$, we have the same excitation energies. We can see that the excitation energies of 3_1^- state split into the three groups. It is numerical error due to the symmetries with 3D Cartesian mesh. The numerical error is less than 0.1 keV. That is, in our calculation for spherical nuclei, the excitation energies with quantum number $(-,+,+)$, $(+,-,+)$ and $(+,+,-)$ are same and the excitation energies with quantum number $(+,-,-)$, $(-,+,-)$ and $(-,-,+)$ are same. Similarly, in our calculation for the deformed nuclei which shape is axial symmetric around z-axis, the excitation energies with quantum number $(-,+,+)$ and $(+,-,+)$ are same and the excitation energies with quantum number $(+,-,-)$ and $(-,+,-)$ are same. Therefore, we calculate only one of those for each case.

Table 4.4: The lowest three excitation energies (in MeV) with quantum numbers $(s_x^\lambda, s_y^\lambda, s_z^\lambda)$ for odd parity states of ^{16}O. The employed interaction is SIII. Parentheses in the second, third and forth column represent the number of iterations. The mesh size is 1.0 fm and the number of mesh points is 20 for one direction in the calculation.

$(s_x^\lambda, s_y^\lambda, s_z^\lambda)$	$\hbar\omega_1$	$\hbar\omega_2$	$\hbar\omega_3$
$(-,+,+)$	$0.51982602i$ (290)	6.46756432 (205)	6.52047684 (169)
$(+,-,+)$	$0.51982602i$ (290)	6.46756433 (196)	6.52047683 (143)
$(+,+,-)$	$0.51982615i$ (290)	6.46756432 (272)	6.52047684 (140)
$(-,-,-)$	6.52563533 (200)	8.19526708 (189)	8.19526708 (256)

4.3 Method for accurately calculating in the mesh representation

In this section, we explain that we can obtain accurate numerical results even if a rather coarse mesh is used in the calculation [33].

We perform the HF plus RPA calculations on the two types of 3D Cartesian meshes with even and odd number of mesh points in one-direction (see Fig. 4.2). Then, we take an average of the numerical results obtained on each of two types of meshes. This procedure provides us with the accurate results even when rather coarse mesh size is employed.

In both meshes of Figs. 4.2 (a) and (b), we employ points inside a cube. When we impose the spatial symmetries on the wave functions in terms of Eq. (4.35), the possible mesh is one of the who meshes provided that the center of the nucleus coincide with the center of the cubic mesh space. Hereafter, we call the mesh in Fig. 4.2 (a) the even-mesh and the mesh in Fig. 4.2 (b) the odd-mesh.

As illustrative examples, the method is applied to ^{16}O in HF and RPA calculations, where the number of mesh points is fixed to 30^3 in even-mesh calculation and 31^3 in odd-mesh calculation. The calculations are carried out with the mesh size being changed from 1.0 fm to 0.6 fm by step-size 0.02 fm. Also numerical results by means of Lagrange mesh (LM) method and 9-point formula of finite-difference (FD) method which are used in order to approximate differential operators, are compared. The employed interaction is SIII except $\theta_{J^2} = 1$ (see Table 4.1), that is, the $\overleftrightarrow{J}^2$ terms in Skyrme energy functional are included in the calculation.

Fig 4.3 shows mesh size dependence of total binding energy of ^{16}O. Fig 4.3

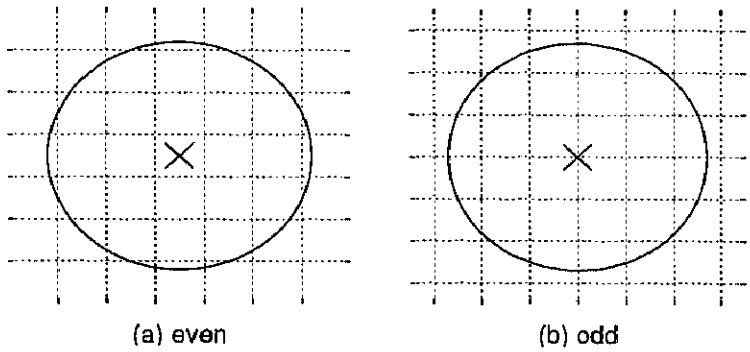

Figure 4.2: Schematic illustration of two ways of setting the mesh on space. The intersection points of dotted lines represent mesh points. Each circle represents a nucleus, whose center of mass is marked by a cross ($\times$). The center of mass of a nucleus is located at the middle point of the mesh points in (a) and coincides with a mesh point (the origin) in (b).

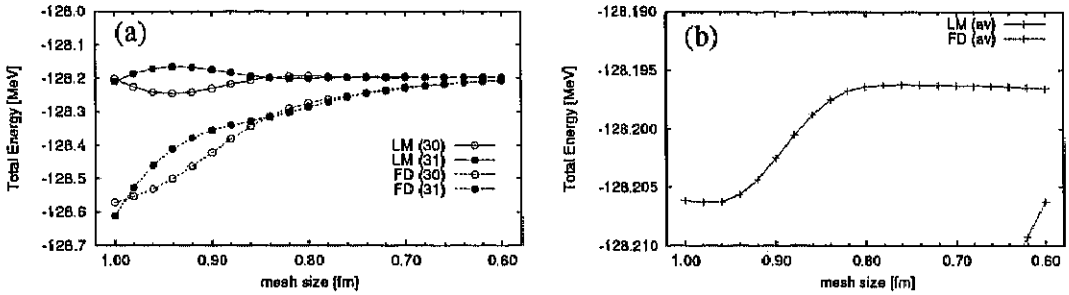

Figure 4.3: Mesh size dependence of total energy of ^{16}O. Open (filled) circles in (a) denote numerical results with the even-mesh (odd-mesh) calculation where 30^3 (31^3) mesh points are used. Plus signs in (b) are averages of the even-mesh and the odd-mesh calculations at each mesh size. Lines (dotted lines) represent the calculation with Lagrange mesh method (9-point formula of finite difference method).

(a) represents numerical results with even-mesh and odd-mesh calculations and Fig. 4.3 (b) is for the averages of both results. LM (FD) stands for Lagrange mesh (finite difference) method. In Fig 4.3 (a), it is seen that the total binding energy of each case converges to a value -128.2 MeV as the mesh size goes smaller. The results with LM method are better than that with FD method at each mesh size. In Fig 4.3 (b), we can see that the deviation of the averages with Lagrange mesh method is within 10 keV at each mesh size.

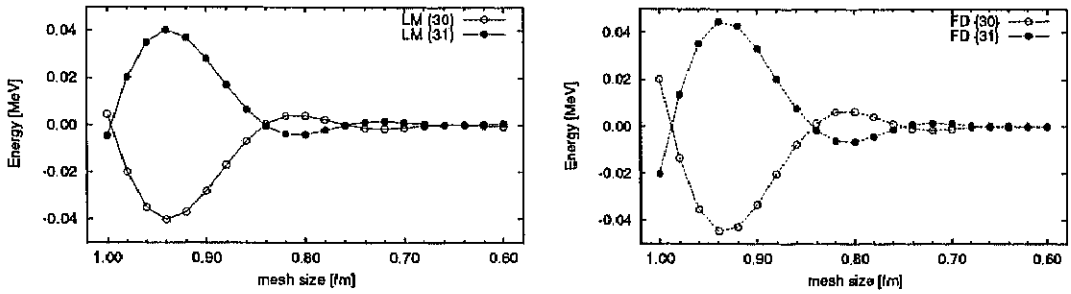

Figure 4.4: Deviation of the total energy of ^{16}O from the average. The notations are the same as in Fig. 4.3.

Fig 4.4 shows the mesh size dependence of a deviation of the total energy of ^{16}O from the average. The left figure of Fig. 4.4 is with Lagrange mesh method and the right figure with finite difference (FD) method. We can see that the results with LM method is similar to that with FD method. Therefore, difference of the averages of LM method and FD method in Fig 4.3 mainly originates from a numerical error due to the approximation of the differential operator.

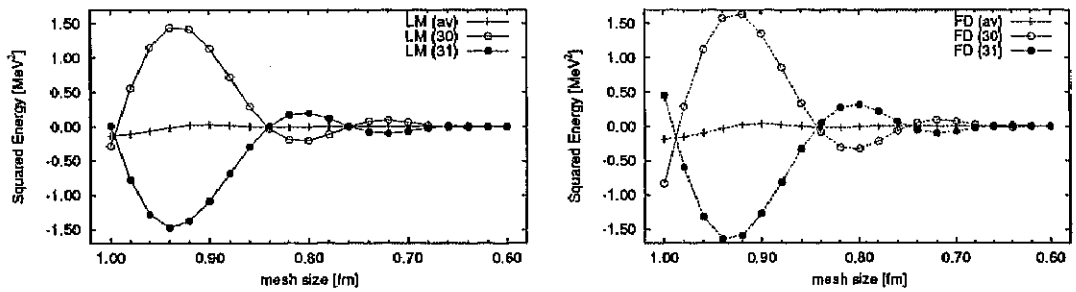

Figure 4.5: Squared energy for spurious state of ^{16}O. The notations are the same as in Fig. 4.3.

Fig. 4.5 shows mesh size dependence of the squared energies $(\hbar\omega_\lambda)^2$ for spurious state of ^{16}O. The left figure of Fig. 4.5 is with LM method and the right figure with FD method. We can see that the results with LM method is similar to that with FD method. We can also see that the results in Fig. 4.5 is similar to that in Fig. 4.4 except sign. When the total energy with one mesh is lower (higher) than the average of total energy with the even-mesh and the odd-mesh, the squared energy of computational spurious state is positive (negative) for both LM and FD cases. We can not predict which of the squared energy is positive or negative when we determine the number of mesh points. The average of the results of the two mesh calculations is close

to the converged value, that is, zero for all over the mesh point in both LM and FD cases.

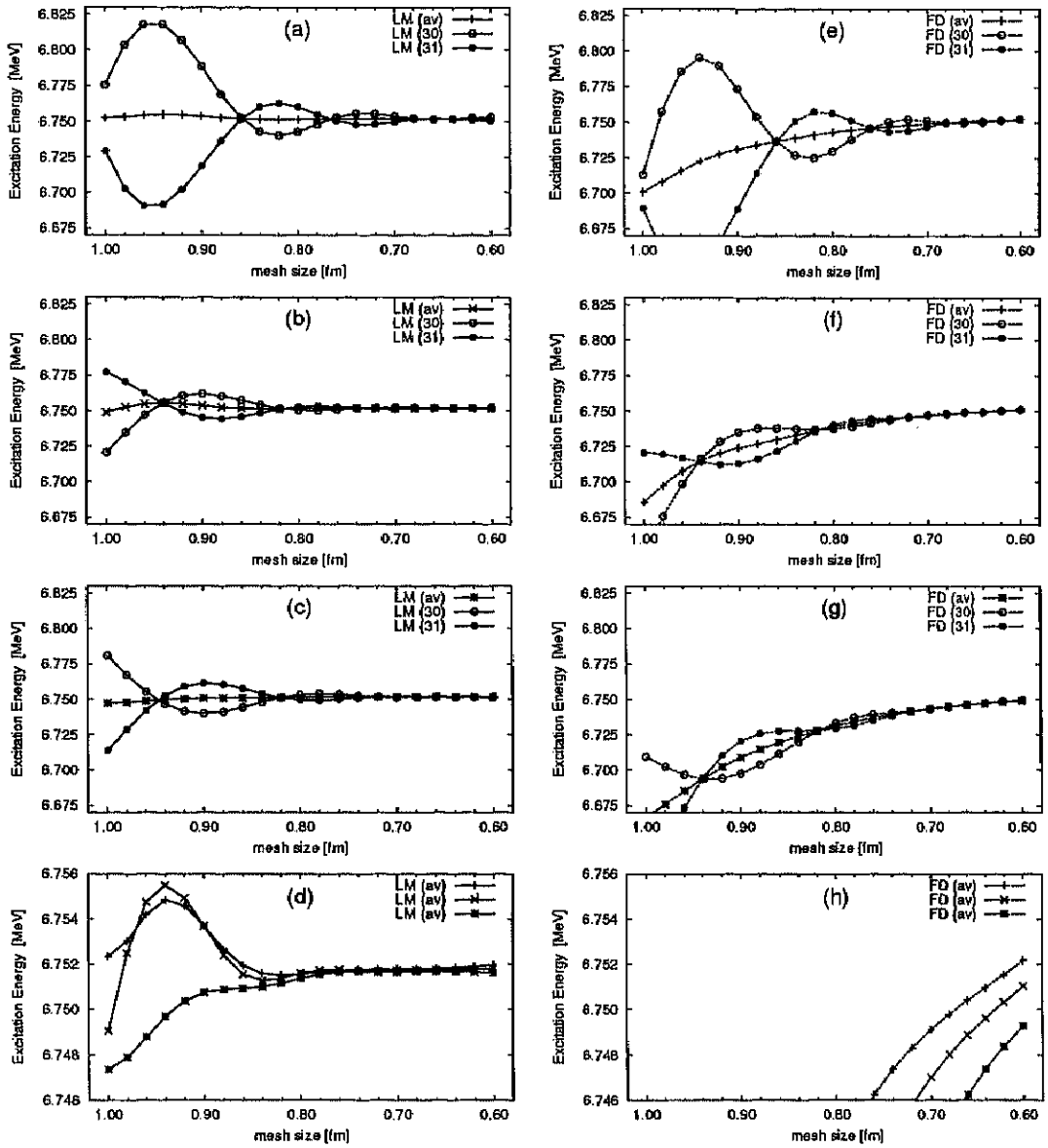

Figure 4.6: Excitation energy for 3_1^- of ^{16}O. The notations are the same as in Fig. 4.3. See the text for the meaning of the panels from (a) to (h).

In Figs. 4.6 and 4.7, we show the excitation energies and the reduced electric-octupole transition probabilities for first 3_1^- state of ^{16}O. As explained in the Table 4.4, the seven degenerate excitation energies split into three

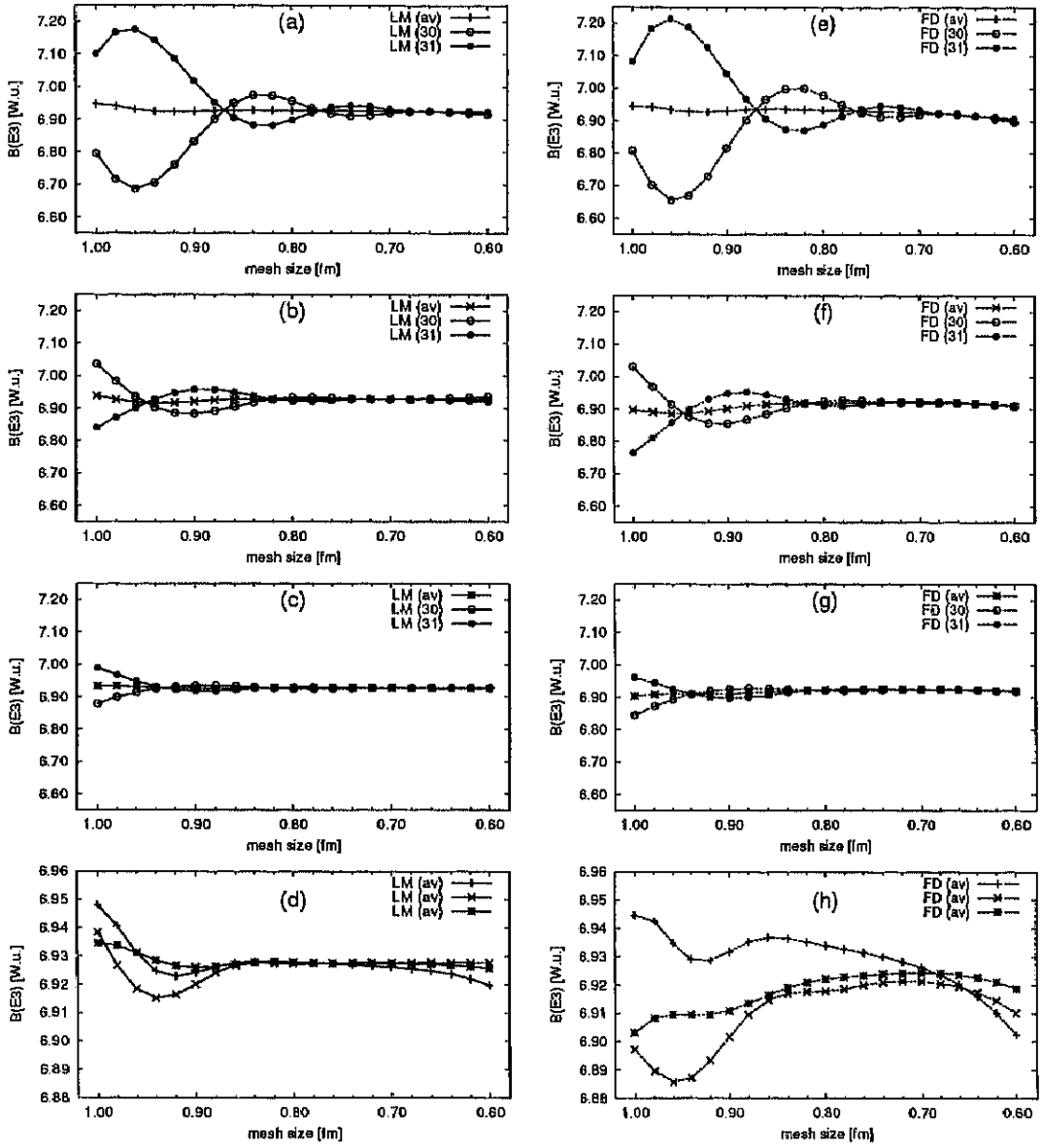

Figure 4.7: Reduced transition probability B(E3) for 3_1^- of ^{16}O. The notations are the same as in Fig. 4.6.

groups: In the first group, there are three components, where each transition amplitude is proportional to $\widetilde{Y}_{30}\rho^{\lambda} \sim z(5z^2 - 3r^2)\rho^{\lambda}$ and its permutations of x, y and z, i.e., $x(5x^2 - 3r^2)\rho^{\lambda}$ and $y(5y^2 - 3r^2)\rho^{\lambda}$. In the second group, there are three components, where each transition amplitude is proportional to $\widetilde{Y}_{32}\rho^{\lambda} \sim z(y^2 - x^2)\rho^{\lambda}$ and its permutations of x, y and z, i.e., $x(z^2 - y^2)\rho^{\lambda}$ and $y(x^2 - z^2)\rho^{\lambda}$. In the third group, there is one component, where the transition amplitude is proportional to $\widetilde{Y}_{3-2}\rho^{\lambda} \sim xyz\rho^{\lambda}$. Here, we use the modified spherical harmonics $\widetilde{Y}_{lm}$ in Eqs. (4.45) and transition density $\rho^{\lambda}(r)$ in Eq. (3.18a). The (a) and (e) in the Figs. 4.6 and 4.7 are the results of the first group with LM and FD method. The (b) and (f) in the Figs. 4.6 and 4.7 are the results of the second group with LM and FD method. The (c) and (g) in the Figs. 4.6 and 4.7 are the results of the third group with LM and FD method. The (d) and (f) in the Figs. 4.6 and 4.7 are the results of the average of the even-mesh and odd-mesh calculations for each of the three groups with LM and FD method. In Fig. 4.6 (4.7), as the mesh size goes smaller, excitation energies (reduced transition probabilities) with the even-mesh and odd-mesh converge to a value 6.752 MeV (6.93 Weisskopf unit). The excitation energies with LM method is better than those with FD method. However,the transition probability with LM method is similar to those with FD method. The average of excitation energies (reduced transition probability) of even-mesh and odd-mesh calculations with Lagrange mesh is within 10 keV (0.04 W.u.) for all of the displayed mesh size.

In Table 4.5 shows squared energies of spurious state of rotation on the top of triaxial superdeformed state of ^{40}Ca, which is explained in chapter 6. The Lagrange mesh method is used in the calculations. We can see that the average of even-mesh and odd-mesh calculations is very close to zero. That is, we can calculate the accurate results in the case of triaxial nuclei.

Thus, we can obtain the accurate results of excitation energies and reduced transition probabilities by means of the above averaging method and Lagrange mesh method.

4.4 Correlation energy of spurious motion

In this section, we explain that the correction energy due to the spurious vibration can be approximately calculated in terms of the computational spurious states. According to our formulation of SHF plus RPA, we can obtain the computational spurious state with finite eigenvalue.

Using the wave function $\phi_i^{(\pm)\lambda}(x)$ in Eq. (2.45), the correlation energy of

Table 4.5: Squared energies of spurious state of rotation on the top of superdeformed state of ^{40}Ca. First row represent quantum number in Eq. (4.68). The squared energies is given in MeV^2. The numbers in parentheses of second column represent the number of mesh points in one-direction. The "av" in parentheses of second column represent average of the values of (25) and (26). "0.8 fm" in second column represent mesh size used in the calculation.

	$(s_x^\lambda, s_y^\lambda, s_z^\lambda)$	$(+,-,-)$	$(-,+,-)$	$(-,-,+)$
	0.8 fm (25)	0.07107	-0.03451	0.03640
SIII	0.8 fm (26)	-0.06862	0.03676	-0.03535
	0.8 fm (av)	0.00122	0.00112	0.00052
	0.8 fm (25)	0.02148	-0.01301	0.00114
Z_σ	0.8 fm (26)	-0.02142	0.01406	-0.00093
	0.8 fm (av)	0.00003	0.00053	0.00010
	0.8 fm (25)	0.09372	-0.02998	0.01070
SkX	0.8 fm (26)	-0.09147	0.03334	-0.01361
	0.8 fm (av)	0.00113	0.00168	-0.00145
	0.8 fm (25)	0.00445	-0.00910	-0.00215
SkI4	0.8 fm (26)	-0.00556	0.01031	0.00490
	0.8 fm (av)	-0.00056	0.00060	0.00137
	0.8 fm (25)	0.04346	-0.01738	0.00866
SkO	0.8 fm (26)	-0.04299	0.01859	-0.00992
	0.8 fm (av)	0.00024	0.00061	-0.00063

certain mode λ in Eq. (2.44) is written for the physical mode as

$$\hbar\omega_\lambda \sum_{ix} \left|Y_i^\lambda(x)\right|^2 = \frac{1}{4}\hbar\omega_\lambda \sum_{ix} \left|\phi_i^{(+)\lambda}(x) - \phi_i^{(-)\lambda}(x)\right|^2, \tag{4.70}$$

and written for the spurious mode as

$$\frac{1}{2M_\lambda} \sum_{ix} \left|P_i^\lambda(x)\right|^2 = \frac{1}{4}|\hbar\omega_\lambda| \sum_{ix} \left|\phi_i^{(+)\lambda}(x)\right|^2. \tag{4.71}$$

For the case of the pure imaginary eigenvalue, we assume the correlation energy of Eq. (4.70) to become the following equation:

$$|\hbar\omega_\lambda| \sum_{ix} \left|Y_i^\lambda(x)\right|^2 = \frac{1}{4}|\hbar\omega_\lambda| \sum_{ix} \left|\phi_i^{(+)\lambda}(x) - \phi_i^{(-)\lambda}(x)\right|^2. \tag{4.72}$$

Since computational spurious state has finite eigenvalue, in order to evaluate the correlation energy of the spurious state in terms of the wave function $\phi_i^{(\pm)\lambda}(x)$, one may expect the correlation energy of Eq. (4.72) is better than the ones of Eq. (4.71) at least for the real eigenvalue. However, the fact is the opposite.

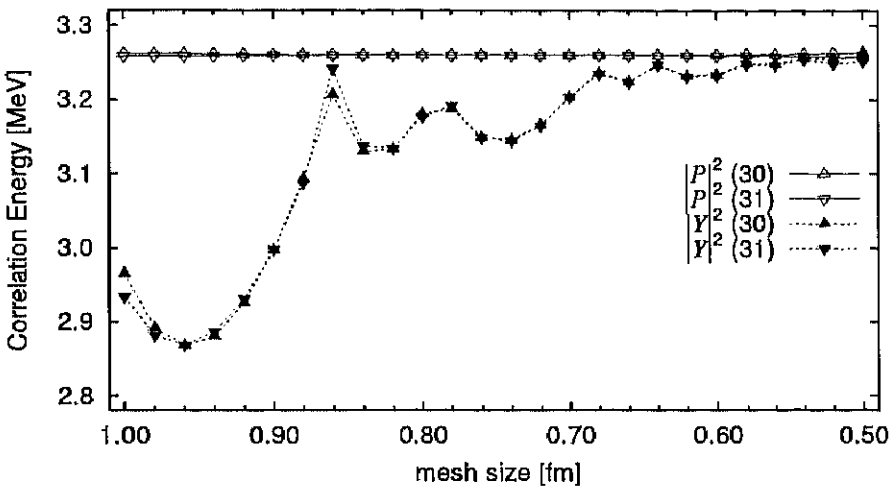

Figure 4.8: Correlation energy corresponding to the center-of-mass spurious vibration for ^{16}O. The transition density has odd symmetry with respect to the $z = 0$-plane. The used Skyrme interaction is Z_σ. The number in the parenthesis represents the number of mesh points for one direction used in the calculation. $|P|^2$ represents the results with the right-hand-side of Eq. (4.71) and $|Y|^2$ represents the results with the left-hand-side of Eq. (4.70).

In Fig. 4.8, we show the correlation energy corresponding to the center-of-mass spurious vibration for ^{16}O. The transition density has odd symmetry with respect to the $z = 0$-plane. We can see that the correlation energy of Eq. (4.70) converges only in the small mesh size region except for the 0.86 fm, and the correlation energy of Eq. (4.71) converges for all of the displayed mesh size region. Rewriting Eq. (4.72) into

$$|\hbar\omega_\lambda| \sum_{ix} \left|Y_i^\lambda(x)\right|^2 = \frac{1}{4}|\hbar\omega_\lambda| \sum_{ix} \left[\left|\phi_i^{(+)\lambda}(x)\right|^2 + \left|\phi_i^{(-)\lambda}(x)\right|^2\right] - |\hbar\omega_\lambda|, \quad (4.73)$$

the differences between Eq. (4.71) and Eq. (4.72) are the second term and the third term in the right-hand side of Eq. (4.73). We confirm the second term is much smaller than the third term for all of the displayed mesh size

region. In other words, the differences between Eq. (4.71) and Eq. (4.72) just coincide with the absolute value of the excitation energy of the computational spurious state. Thus, if the excitation energy of computational spurious state is very small, then the correlation energy in Eq. (4.72) gives the accurate values. After all, we should use Eq. (4.71) in order to evaluate the correlation energy.

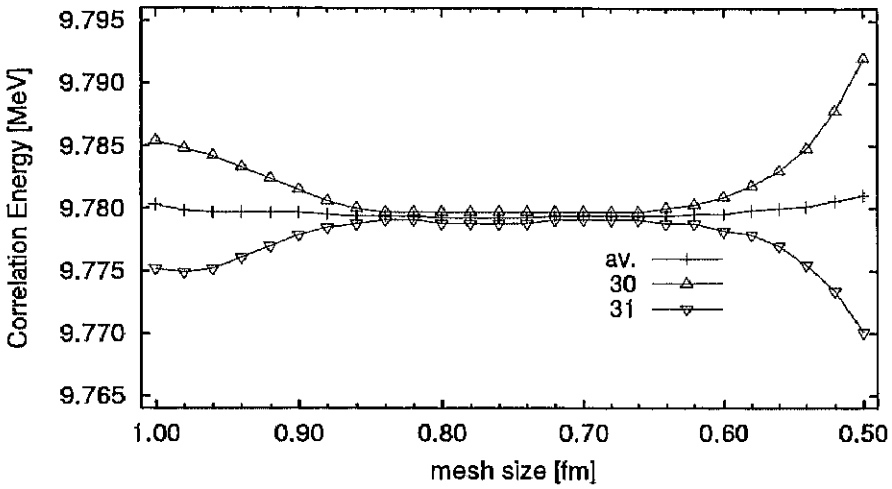

Figure 4.9: RPA correlation energy of the center-of-mass vibration for ^{16}O. The number "30" and "31" represents the number of mesh points for one-direction used in the calculation. The "av." represents the average of the results of "30" and "31".

The RPA correlation energy of the center-of-mass vibration coincides with the HF expectation value of the center of mass motion:

$$\sum_{\lambda \in \text{c.m.}} \frac{1}{2M_\lambda} \sum_{ix} \left| P_i^\lambda(x) \right|^2 = \frac{1}{2Am} \langle \text{HF} | \hat{P}^2_{\text{c.m.}} | \text{HF} \rangle, \tag{4.74}$$

where the label "c.m." in summation represents the summation over spurious center of mass vibration. We show the RPA correlation energy of the center-of-mass vibration calculated with the right-hand-side of Eq. (4.71) in Fig. 4.9. We also show the HF expectation value of the center of mass motion calculated with the right-hand side of Eq. (4.74) in Fig. 4.10. We can see in both figures that the influence of the box size used in the calculation is not ignored in the region where the mesh size is smaller than 0.6 fm. Though, the values labelled "av" in both figure are almost constant for all of the mesh size region. The difference between the values labelled "av." in Fig. 4.9 and those

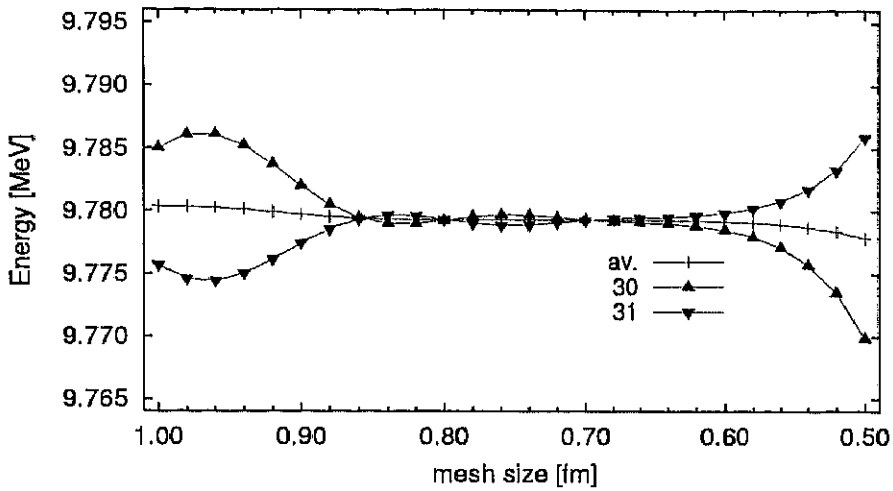

Figure 4.10: The HF expectation value of the center-of-mass motion for ^{16}O. The labels are the same as Fig. 4.9.

in Fig. 4.10 is within a few keV for all of the mesh size region. Furthermore, the situation is all the same in the deformed nuclear case. For example, the difference between RPA correlation energy of the center-of-mass vibration and the HF expectation value of the center-of-mass motion is 3 keV for the 8p-8h superdeformed state of ^{40}Ca, where the mesh size of 0.8 fm and 25 and 26 mesh points are used in the calculations. Therefore, in our numerical calculation, we can assert that the the RPA correlation energy of the center-of-mass vibration coincides with the HF expectation value of the center of mass motion.

The same argument can be applied to the case of the spurious rotational motion. Then, the RPA correlation energy of spurious rotational motion coincides with the HF expectation value of rotational motion:

$$\frac{1}{4}|\hbar\omega_\lambda|\sum_{ix}\left|\phi_i^{(+)\lambda}(x)\right|^2 = \frac{1}{2\mathcal{J}_\nu}\langle \mathrm{HF}|\hat{J}_\nu^2|\mathrm{HF}\rangle, \tag{4.75}$$

where the $\hat{J}_\nu$ is total angular momentum operator around ν-axis and the $\mathcal{J}_\nu$ is the moment of inertia around ν-axis, which corresponds to the Thouless-Valatin formula for moment of inertia [64] (cf. [47]). $\phi_i^{(+)\lambda}$ is the RPA wave function, which is following state with the quantum number $(s_x^\lambda, s_y^\lambda, s_z^\lambda)$:

- $\nu = x \longrightarrow$ spurious state with the quantum number $(+,-,-)$
- $\nu = y \longrightarrow$ spurious state with the quantum number $(-,+,-)$

- $\nu = z \longrightarrow$ spurious state with the quantum number $(-,-,+)$

Of course, these states do not exist when the nuclear shape is axial around ν-axis. Then, the RPA correlation energy of spurious rotational motion does not exist.

4.5 Comparison with other calculations

In this section, we compare our numerical results with those by other groups. We perform the three-dimensional Cartesian mesh calculation with Lagrange mesh method, and our results in this section are obtained by the averaging method explained in previous section 4.3.

4.5.1 HF calculations

Since the RPA calculation are based on the HF single-particle states, we start with confirming the accuracy of our HF calculation with Lagrange mesh method.

Table 4.6: Binding energies (in MeV) of several spherical nuclei. The used numerical method are a spherical oscillator basis (SHOB) [8], a spherical radial mesh (RM) [26], a three-dimensional Cartesian mesh with finite difference approximation (3DM) [26], and a three-dimensional Cartesian mesh with the Lagrange mesh method (3DLM). Our results are shown in the last two rows. The Skyrme SIII force is used in all of the calculations. Parentheses in first column represents a mesh size used in each calculation.

	^{16}O	^{40}Ca	^{90}Zr	^{208}Pb
SHOB	128.21	341.85	782.66	1636.61
RM (0.1 fm)	128.27	341.92	782.73	1636.61
3DM (0.8 fm)	128.26	341.86	783.12	1638.43
3DM (1.0 fm)	128.74	343.32	786.14	1645.19
3DLM (0.8 fm)	128.202	341.849	782.566	1636.372
3DLM (1.0 fm)	128.212	341.851	782.571	1636.379

Table 4.6 shows the binding energies of several spherical nuclei calculated with four types of numerical methods. It is pointed out in Ref. [26] that the relative error of binding energy in three-dimensional Cartesian mesh calculation using coarse mesh size (1.0 fm), where finite difference formula is used

to approximate differential operator, is about 0.5% and cannot be negligible for medium and heavy nuclei. So, one should correct the binding energy for this small numerical inaccuracy in the case of the usual 3D mesh calculation. One can see that the relative error of the binding energy is very small of the order of keV even if coarse mesh size (1.0 fm) is used when the 3D Cartesian mesh calculation with Lagrange mesh is employed. Thus it is not necessary to mind numerical error in the case of the 3D Cartesian mesh calculation with Lagrange mesh.

4.5.2 RPA calculations

Spherical nuclei

In order to demonstrate our RPA calculation is correct, we compare our calculations with the ones of Refs. [19, 20, 65]. In Refs. [19, 20], the calculation was performed with the spherical harmonic oscillator basis and the Coulomb interaction was neglected in the RPA calculation. In Ref. [65], the calculation was performed using the response function method (continuum RPA) [17, 32].

Table 4.7: The excitation energies for 3^-_1 states of doubly magic nuclei with Skyrme SIII force. Our calculation is performed with the original Skyrme parameters SIII except $\theta_{J^2} = 1$. The energies are given in MeV. The last row with Exp shows the experimental values.

	^{16}O	^{40}Ca	^{90}Zr	^{208}Pb
our results	6.75	2.49	1.07	2.24
Blaizot and Gogny [19]	6.77	2.76	1.57	2.82
Krewald *et al.* [20]	7.04	—	—	3.33
Abbas *et al.* [65]	6.86	3.90	1.59	2.98
Exp [66]	6.13	3.74	2.75	2.62

In Table 4.7, we show our numerical results of the excitation energies for the 3^-_1 states of spherical nuclei with Skyrme SIII force. As a comparison, the numerical results of other groups' [19, 20, 65] and experimental values [66] are also listed. In each case of the listed nuclei, our excitation energy is smaller than the others'. Because our calculation is considered as continuum RPA calculation, our numerical results should be lower than those of Refs. [19, 20], whose calculations are carried out with the truncated harmonic oscillator basis and do not include the continuum effect. On the other hand,

in Ref. [65], the response function method is employed and the continuum is properly treated in the calculations. From the viewpoint of the continuum RPA, our method of calculation is essentially the same as the one in Ref. [65], since the RPA equations are formulated and solved in the mixed configuration space of coordinate and hole orbitals. But the difference between our results and those of Ref. [65] is not small. The results of Ref. [65] are a bit larger than those of Ref. [19] for ^{16}O, ^{90}Zr, ^{208}Pb, and somewhat larger for ^{40}Ca. If the same interaction is used, the results of Ref. [65] should be smaller than those of Ref. [19]. Therefore, the interaction used in Ref. [65] may be different from that used in Ref. [19], for example, in the treatment of the Coulomb interaction, the spurious state, and $(\boldsymbol{\sigma}\cdot\boldsymbol{\sigma})$ terms or $(\boldsymbol{\sigma}\cdot\boldsymbol{\sigma})(\boldsymbol{\tau}\cdot\boldsymbol{\tau})$ terms and so on.

In Table 4.8, we compare our results and the ones by Blaizot and Gogny in detail with respect to the properties of 3^-_1 states of the spherical nuclei. In the table, label "BG" is used for the numerical results by Blaizot and Gogny [19]. Our calculations are performed in three cases, (i), (ii) and (iii), for each of the Skyrme parameters SIII and SIV. A case (i) is the same as original Skyrme parameters. A case (ii) is the same as original Skyrme parameters except $\theta_{J^2} = 1$. A case (iii) is the same as the case (ii) but the Coulomb interaction is neglected in the RPA calculation.

One can confirm that the effect of the parameter θ_{J^2} by comparing the results of (i) and (ii). It is clear that the effect of this parameter is not negligible for the excitation energy and the reduced transition probability. One can also confirm the contribution of the Coulomb interaction by comparing the results of (ii) and (iii). The RPA calculation with the case (iii) is not selfconsistent because of the removal of Coulomb interaction in the RPA calculation. It is seen that the contribution of the Coulomb force to the reduced transition probability is large in heavy nuclei, in which the Coulomb force is large.

Seeing the binding energy and the single particle gap in the Table 4.8, it is clear that the calculations by Blaizot and Gogny were performed in the case (ii) (or (iii), where the binding energy and the single-particle gap are equal to the ones in the case (ii)). For ^{16}O, the excitation energies of the case (ii), whose values are 6.75 MeV for SIII and 8.88 MeV for SIV, agree with the results of BG, whose values are 6.77 MeV for SIII and 8.9 MeV for SIV. The excitation energies of the case (iii), whose values are 6.74 MeV for SIII and 8.87 MeV for SIV, also coincide with those of BG too. The excitation energies of the other nuclei in the case (ii) are smaller than those of BG respectively, and the reduced transition probability B(E3) of all nuclei in the case (ii) are larger than those of BG respectively. These tendencies are larger for the case (iii). We do not understand the origin of these discrepancy. One

Table 4.8: Comparison of properties of the low-lying collective 3_1^- states for doubly magic nuclei between our results and the ones by Blaizot and Gogny [19]. Our calculations are performed for three different cases: The case (i) is the same as the original Skyrme parameters. The case (ii) is the same as the original Skyrme parameters except $\theta_{J^2} = 1$. The case (iii) is the same as the case (ii) but the Coulomb contribution is neglected in the RPA calculation. The "BG" represents the results by Blaizot and Gogny. E/A is binding energy per nucleon. $\Delta_{\rm sp}$ is the average single particle gap: $\Delta_{\rm sp} = \frac{1}{2}(\Delta_{\rm sp}^{\rm protons} + \Delta_{\rm sp}^{\rm protons})$. $E_x(3_1^-)$ is excitation energy given in MeV and $B(E3)$ is reduced transition probability in Weisskopf units for 3_1^- states.

		^{16}O				^{40}Ca			
		E/A	$\Delta_{\rm sp}$	$E_x(3_1^-)$	B(E3)	E/A	$\Delta_{\rm sp}$	$E_x(3_1^-)$	B(E3)
SIII	(i)	-8.01	7.61	6.49	6.67	-8.55	5.54	2.39	31.0
	(ii)	-8.01	7.65	6.75	6.93	-8.55	5.54	2.49	28.7
	(iii)	-8.01	7.65	6.74	6.98	-8.55	5.54	2.40	30.6
	BG	-8.00	7.7	6.77	6.23	-8.53	5.61	2.76	22.7
SIV	(i)	-8.03	11.11	8.60	10.9	-8.54	8.55	2.93	49.7
	(ii)	-8.03	11.20	8.88	11.2	-8.54	8.59	3.15	46.5
	(iii)	-8.03	11.20	8.87	11.2	-8.54	8.59	3.00	49.7
	BG	-8.02	11.2	8.9	10.1	-8.52	8.65	3.48	38.4

		^{90}Zr				^{208}Pb			
		E/A	$\Delta_{\rm sp}$	$E_x(3_1^-)$	B(E3)	E/A	$\Delta_{\rm sp}$	$E_x(3_1^-)$	B(E3)
SIII	(i)	-8.70	3.48	0.97	48.5	-7.87	3.63	2.44	43.9
	(ii)	-8.66	3.24	1.07	45.2	-7.84	3.28	2.24	44.1
	(iii)	-8.66	3.24	0.86	60.6	-7.84	3.28	2.04	52.8
	BG	-8.64	3.21	1.57	28	-7.80	3.39	2.82	33
SIV	(i)	-8.69	5.73	2.30	56.1	-7.87	5.52	3.10	49.4
	(ii)	-8.64	5.39	2.34	56.7	-7.83	5.03	2.86	51.2
	(iii)	-8.64	5.39	2.08	66.7	-7.83	5.03	2.61	59.6
	BG	-8.62	5.33	2.81	45	-7.80	5.15	3.48	44

of the possible origin is the fact that our calculation does not impose any truncation on the particle orbitals, whereas Blaizot and Gogny did.

Table 4.9: Comparison of properties of spurious, 3^-_1 and 2^-_1 state for ^{16}O between our results and the ones by Krewald *et al.* [19]. Our calculations are performed in three cases: The case (i) is the same as the original Skyrme parameters except $\theta_{J^2} = 1$. The case (ii) is the same as the original Skyrme parameters except $\theta_{J^2} = 1$ and $\theta_{C_{ex}} = 1$. The case (iii) is the same as the case (ii) but the Coulomb interaction is neglected in the RPA calculation. The rows labeled "Kr" show the results by Krewald *et al.*. $E_{\rm spu}$ is the energy of spurious state. $E_x(3^-_1)$ is excitation energy and $B(E3)$ reduced transition probability for 3^-_1 states. $E_x(2^-_1)$ is excitation energy and $B(M2)$ reduced transition probability for 2^-_1 states. $\pi d_{5/2}p^{-1}_{1/2}$ and $\pi d_{5/2}p^{-1}_{3/2}$ are particle-hole energy for proton respectively. The energies are given in MeV, and the reduced transition probabilities are given in Weisskopf units.

		^{16}O						
		$E_{\rm spu}$	$E_x(3^-_1)$	B(E3)	$E_x(2^-_1)$	B(M2)	$\pi d_{5/2}p^{-1}_{1/2}$	$\pi d_{5/2}p^{-1}_{3/2}$
SII	(i)	$0.02i$	9.54	9.13	12.12	0.203	11.29	16.60
	(ii)	$0.01i$	9.51	9.33	12.07	0.264	11.23	16.50
	(iii)	$2.32i$	9.45	9.52	12.07	0.264	11.23	16.50
	Kr	1.80	9.82	8.90	12.15	0.159	11.24	16.51
SIII	(i)	$0.07i$	6.75	6.93	8.35	0.326	7.58	13.49
	(ii)	$0.07i$	6.74	7.09	8.33	0.373	7.56	13.43
	(iii)	$2.31i$	6.71	7.25	8.33	0.373	7.56	13.43
	Kr	2.60	7.04	6.38	8.39	0.305	7.54	13.45
SV	(i)	$0.05i$	10.54	12.74	15.27	0.334	13.76	21.69
	(ii)	$0.05i$	10.50	13.01	15.17	0.508	13.65	21.52
	(iii)	$2.35i$	10.47	13.30	15.17	0.508	13.65	21.52
	Kr	0.50	10.86	13.1	15.3	0.242	13.67	21.54

Table 4.9 shows comparison of properties for spurious, 3^-_1 and 2^-_1 states of ^{16}O between our results and the ones by Krewald *et al.* [20]. Our calculations are performed with three cases, (i), (ii) and (iii), for each of the Skyrme parameters, SII, SIII and SV. A case (i) is the same as original Skyrme parameters except $\theta_{J^2} = 1$. A case (ii) is the same as original Skyrme parameters except $\theta_{J^2} = 1$ and $\theta_{C_{ex}} = 1$. A case (iii) is the same as the case (ii) but the Coulomb interaction is neglected in the RPA calculation.

Comparing the results of (ii) and (iii), we can see that the removal of the Coulomb force in the RPA calculation strongly affects spurious states and weakly affects 3_1^- state and do not affects 2_1^- state. The reason that the removal of the Coulomb force has no influence on 2_1^- state is that the 2_1^- state is one-particle one-hole excitation and has little dependence on the residual interaction of RPA.

Seeing the particle-hole energies for proton, $\pi d_{5/2}p_{1/2}^{-1}$ and $\pi d_{5/2}p_{3/2}^{-1}$, in the Table 4.9, it is clear that the calculations by Krewald *et al.* were performed for the case (ii) (or (iii)). For each of the Skyrme parameters, the excitation energies and the reduced transition probabilities of 3_1^- state for the case (ii) are rather close to those of Krewald *et al.* and the excitation energies of 2_1^- state for the case (ii) are coincident with those of Krewald *et al.*. The reduced transition probabilities of 2_1^- state of (ii) are roughly equal to those of Krewald *et al.*. The energy of the spurious state of (iii) is different from those of Krewald *et al.* in that our results are pure imaginary in contrast with the real values of Krewald *et al.*. We don't clearly know the reason of discrepancy. For the similar calculation by Blaizot and Gogny [19], the excitation energy of spurious state for ^{40}Ca with Skyrme SIV force is $1.7i$ MeV. Maybe Krewald *et al.* did not use the diagonalization method which enables them to treat imaginary eigenvalue. Anyway, the removal of the Coulomb interaction strongly influences spurious state. In our self-consistent SHF plus RPA calculation, the Coulomb interaction is properly included.

Deformed nuclei

There has probably been no calculation of low-lying excited state without charge exchange for deformed nuclei with SHF+RPA. So, in this subsection, we compare our numerical results of the low-lying states of the light deformed nuclei with those by Takami *et al.* [67, 68], where the parity-projected Skyrme Hartree-Fock method is used.

In Fig. 4.11, we show low-lying isoscalar odd-parity states for ^{20}Ne and ^{24}Mg with our calculation (SHF+RPA) and parity-projected Skyrme-Hartree-Fock method (PPSHF) [67, 68]. We can see that our results comparatively coincide with those by Takami *et al.* even though the results are calculated by completely different formulation.

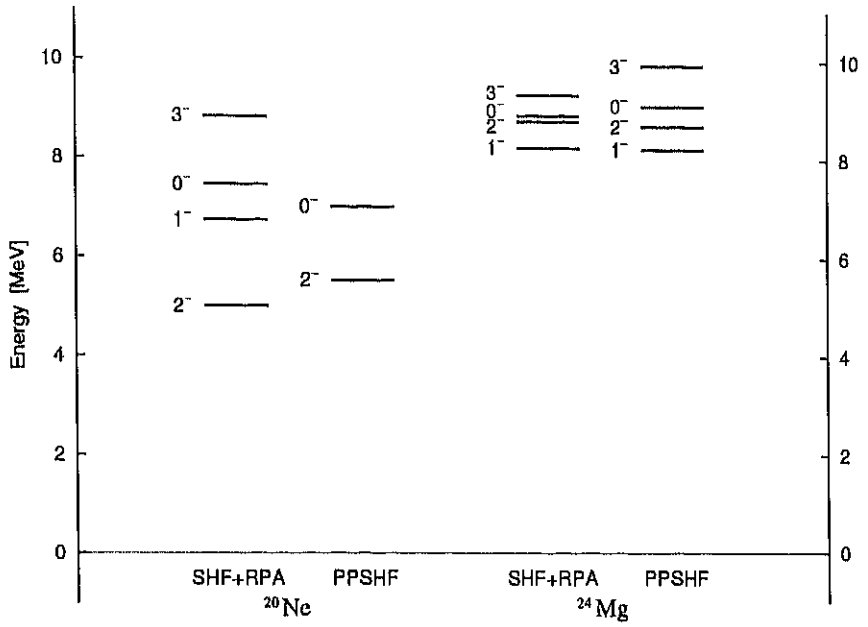

Figure 4.11: Comparison of low-lying isoscalar odd-parity states for ^{20}Ne and ^{24}Mg between our calculation (SHF+RPA) and parity-projected Skyrme-Hartree-Fock method (PPSHF) [67, 68]. Each of the levels are labeled by K^π. Skyrme SGII force is used in both of the methods.

In ^{20}Ne, several rotational bands are observed [69]: One with $K^\pi = 2^-$ built on the the excited $J^\pi = 2^-$ state at 4.97 MeV, one with $K^\pi = 0^-$ built on the excited $J^\pi = 1^-$ state at 5.79 MeV, and the one with $K^\pi = 1^-$ built on the excited $J^\pi = 1^-$ state at 8.85 MeV. In ^{24}Mg, several rotational bands are observed [70]: One with $K^\pi = 0^-$ built on the the excited $J^\pi = 1^-$ state at 7.56 MeV, one with $K^\pi = 3^-$ built on the excited $J^\pi = 3^-$ state at 7.62 MeV, and the one with $K^\pi = 1^-$ built on the excited $J^\pi = 1^-$ state at 8.44 MeV. (K^π for ^{24}Mg is taken from Ref. [71].) We suppose that our results correspond to the band heads of those rotational bands except the $K^\pi = 3^-$ for ^{20}Ne and the $K^\pi = 2^-$ for ^{24}Mg. Thus, in the case of deformed nuclei, our self-consistent SHF plus RPA calculation gives us a firm basis on which we can investigate the low-lying excited state.

4.6 Instability by $s \cdot \triangle s$ term

In this section, we study an unknown instability which occurs in the RPA calculation, induced by $s \cdot \triangle s$ terms in Skyrme energy functional.

It is known instability brought by the three-body term depending on spin density in the Skyrme energy functional [72, 73]. We can explain this instability in terms of the Landau parameters [73], which provides a stability criterion for symmetric unpolarized infinite nuclear matter. The Landau parameters are represented by the coefficients C_t^x in the Skyrme energy functional (3.29) [23]. However, the coefficients $C_t^{\Delta s}$ are not connected with Landau parameters. Therefore, we do not clearly know the mechanism of the instability induced by the $s \cdot \triangle s$ terms. So, we examine the variation of the excitation energy when $C_t^{\Delta s}$ is varied.

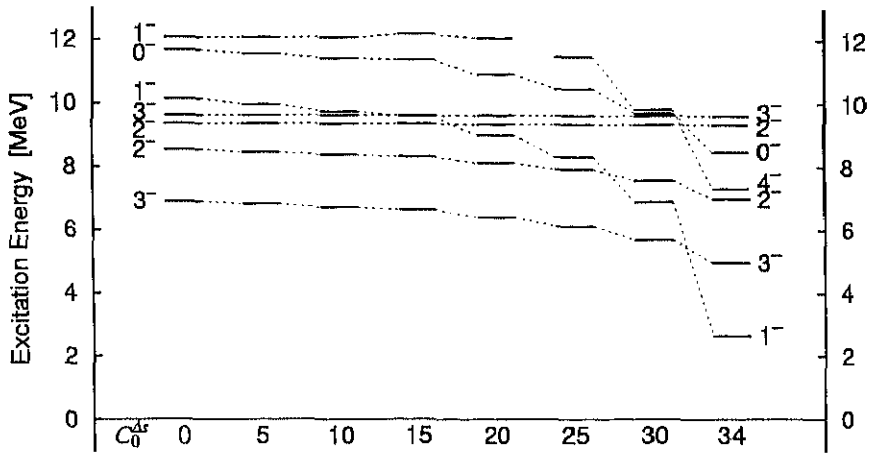

Figure 4.12: Variation of the excitation energy for ^{16}O when $C_0^{\Delta s}$ is varied. The coefficient $C_0^{\Delta s}$ dependence on the excitation spectra for ^{16}O. The Skyrme SIII force is used but we fix $C_1^{\Delta s}$ to zero in the calculation. The original parameter for SIII is $C_0^{\Delta s} = C_1^{\Delta s} = 17.03125$ MeV fm^5.

In Fig. 4.12, we show the variation of the excitation energy for ^{16}O when $C_0^{\Delta s}$ is varied. We can see that the excitation energies of the isovector mode do not vary but those of the isoscalar mode come down when $C_0^{\Delta s}$ increase. The rate of the fall of the excitation energies is largest for isoscalar 1^- state. If $C_0^{\Delta s} = 35$, then the instability occurs and we can no longer solve the RPA equation numerically.

In Fig. 4.13, we show the variation of the excitation energy for ^{16}O when

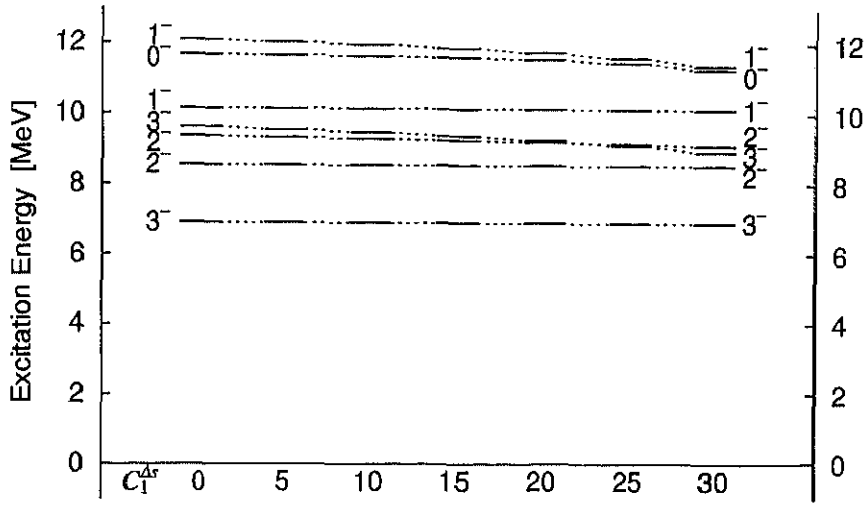

Figure 4.13: Variation of the excitation energy for ^{16}O when $C_1^{\Delta s}$ is varied. The coefficient $C_1^{\Delta s}$ dependence on the excitation spectra for ^{16}O. The Skyrme SIII force is used but we fix $C_0^{\Delta s}$ to zero in the calculation.

$C_1^{\Delta s}$ is varied. In contrast with the case in Fig. 4.12, we can see that the excitation energies of the isoscalar mode do not vary but those of the isovector mode come down when $C_1^{\Delta s}$ increase. For all excitation spectra, the rate of decrease of the excitation energies is much smaller than those in Fig. 4.12.

It is probably that the instability induced with the $C_0^{\Delta s} \boldsymbol{s}_{00} \cdot \Delta \boldsymbol{s}_{00}$ term in the Skyrme energy functional occurs when the isoscalar coefficients $C_0^{\Delta s}$ has large value. In some Skyrme interaction, e.g. SLyx, SkIx, and SkO and so on, such instability actually occurs in our RPA calculation. Therefore, in such case, we remove the $\boldsymbol{s}_{tt_3} \cdot \Delta \boldsymbol{s}_{tt_3}$ terms in the RPA calculation (see section 4.1.1).